Standardizing designed and emergent quantitative features in microphysiological systems

Moerkens, Renée ; Nahon, Dennis M. ; Aydogmus, H.; Lendemeijer, Bas ; Dostanic, M.; Motreuil-Ragot, P.A.; Mastrangeli, Massimo; van der Meer, Andries D. ; Mummery, Christine; More Authors

Important note
To cite this publication, please use the final published version (if applicable).
Please check the document version above.

Standardizing designed and emergent quantitative features in microphysiological systems

Dennis M. Nahon [1,7], Renée Moerkens [2,7], Hande Aydogmus[3], Bas Lendemeijer [4], Adriana Martínez-Silgado[5], Jeroen M. Stein [1], Milica Dostanić[3], Jean-Philippe Frimat[1], Cristina Gontan [4], Mees N. S. de Graaf [1], Michel Hu[1], Dhanesh G. Kasi[1], Lena S. Koch[6], Kieu T. T. Le[2], Sangho Lim[5], Heleen H. T. Middelkamp [6], Joram Mooiweer [2], Paul Motreuil-Ragot[3], Eva Niggl [4], Cayetano Pleguezuelos-Manzano [5], Jens Puschhof[5], Nele Revyn[3], José M. Rivera-Arbelaez[6], Jelle Slager [2], Laura M. Windt[1], Mariia Zakharova[6], Berend J. van Meer [1], Valeria V. Orlova [1], Femke M. S. de Vrij [4], Sebo Withoff[2], Massimo Mastrangeli[3], Andries D. van der Meer [6] & Christine L. Mummery [1] ✉

Microphysiological systems (MPSs) are cellular models that replicate aspects of organ and tissue functions in vitro. In contrast with conventional cell cultures, MPSs often provide physiological mechanical cues to cells, include fluid flow and can be interlinked (hence, they are often referred to as microfluidic tissue chips or organs-on-chips). Here, by means of examples of MPSs of the vascular system, intestine, brain and heart, we advocate for the development of standards that allow for comparisons of quantitative physiological features in MPSs and humans. Such standards should ensure that the in vivo relevance and predictive value of MPSs can be properly assessed as fit-for-purpose in specific applications, such as the assessment of drug toxicity, the identification of therapeutics or the understanding of human physiology or disease. Specifically, we distinguish designed features, which can be controlled via the design of the MPS, from emergent features, which describe cellular function, and propose methods for improving MPSs with readouts and sensors for the quantitative monitoring of complex physiology towards enabling wider end-user adoption and regulatory acceptance.

Microphysiological systems (MPSs) are cellular models that recapitulate aspects of physiology (typically, human physiology) by recreating the dynamic microenvironment to which cells are exposed in organs or tissues. They often integrate features such as gas or liquid flows and are hence often referred to as microfluidic organs-on-chips (OoCs). Their design may also allow the incorporation of mechanical stimulation (such as contraction, stretch or strain) into living tissue constructs. Many MPSs harbour multiple compartments that enable local microenvironments

to be regulated independently to support different cell types while allowing communication between adjacent compartments. This facilitates complex co-culture in a single system and the coupling of multiple MPSs to model multi-organ interactions. The first examples of how these advanced model systems can impact toxicological, pharmaceutical and biomedical science are beginning to emerge[1,2].

With increasing interest in using MPSs, there is a pressing need to develop measurable standards to compare different systems and assess

their in vivo relevance and predictive value. For this, it is essential to quantify physiological features of tissues in MPSs and compare these with actual human (or animal) physiology in vivo. However, although MPSs allow strict control over the culture microenvironment and are thus well suited to quantifying physiological features, most studies to date have only described their qualitative features. Realizing a shift towards quantitative outputs will require control over features such as compartment dimensions, fluid flow rates and oxygen concentration, as well as the monitoring of cellular functions, such as barrier integrity, electrophysiological properties, metabolite production or immune cell recruitment. This will aid the development of measurable standards to qualify systems as fit for purpose (that is, suitable for measuring a parameter of interest) and will improve the reproducibility of models across users. Qualification and standardization will take the technology to the next level and ensure that MPSs become accepted options for regulatory agencies and end users[3].

In this Perspective, we define and categorize quantifiable physiological features as part of the design of the MPS or as a readout of it, provide an overview of the physiological features of the human vascular system, intestine, heart and brain, show how the quantification of physiological features enables the comparison of observations between MPSs and humans in vivo and identify notable technical advances that will probably improve the quantification of physiological features in MPSs.

Quantifiable physiological features for MPSs

Recapitulating specific organ or tissue functions via MPSs involves the use of reverse engineering to incorporate and emulate essential cellular and biophysical components[4,5] on the basis of current understanding of human physiology. We define such components as physiological features. In the context of quantitative modelling, it is helpful to categorize these features as designed or emergent (Fig. 1). Importantly, features are not limited to one of the two groups; they can belong to both, depending on the model and functional readout.

Designed features are physiological features that can be directly controlled via the design of the device (for example, compartment dimensions) or through chemical or mechanical inputs (such as fluid flow dynamics and oxygen concentration). These features can be tightly regulated and are intended to be close mimics of in vivo conditions. Yet, technical limitations in the design or fabrication of the device may constrain whether designed features can be in a physiologically relevant range.

Emergent features are physiological features that describe cellular function. These features (such as the integrity of a cell layer acting as a barrier, the electrophysiological properties of a tissue or the migration of immune cells) cannot be completely controlled—at least not upfront—via device design or input; rather, they arise owing to the intrinsic properties of the cells and the cellular microenvironment in the culture system. Monitoring emergent features in MPSs requires specialized sensors or downstream readouts.

On the one hand, quantification of emergent features in MPSs can indicate physiological relevance and whether a given device design is suitable for the intended application. On the other hand, the quantification of designed features provides insight into how the choice of a design impacts the emergent features and physiological outputs. In addition, quantitative control of the designed features enhances the robustness of MPSs and their reproducibility. Therefore, the quantification of both designed and emergent features is essential if they are to be used (directly or indirectly) in the development of measurable standards of physiological output in MPSs.

The selection of relevant features for any particular MPS depends on the specific research question. In general, the guiding principle is 'as simple as possible, yet as complex as necessary'. This is in line with the widely accepted notion that MPSs should be fit for purpose (that is, an MPS should capture one or a few features rather than serve many of the

conceivable functions or applications)[6]. This means that the designed features incorporated in an MPS should be limited to those necessary to induce the cellular organization and differentiation state required to obtain the physiologically relevant levels of the emergent features being investigated. Similarly, the sensors or readouts used should be limited to those sufficient for monitoring the emergent features of interest. Several causal relationships between designed and emergent features are well established; for example, the oxygen concentration in an intestinal model impacts the diversity of the microbiome. However, most often the exact implications of particular designed features have not been investigated. Quantification of both types of feature in MPSs will be necessary to reveal such relationships and to provide insight into which designed features are required to create useful models for each intended application.

The physiological relevance of MPSs depends on whether the quantified features actually reflect human physiological parameters. In-vitro-to-in-vivo translation requires critical evaluation of the sorts of data that can be collected, how they are measured and normalized and which units might be used. In the following section, we discuss these considerations for the vascular system, intestine, heart and brain and provide deeper understanding of the elements required to create physiologically relevant and fit-for-purpose MPSs.

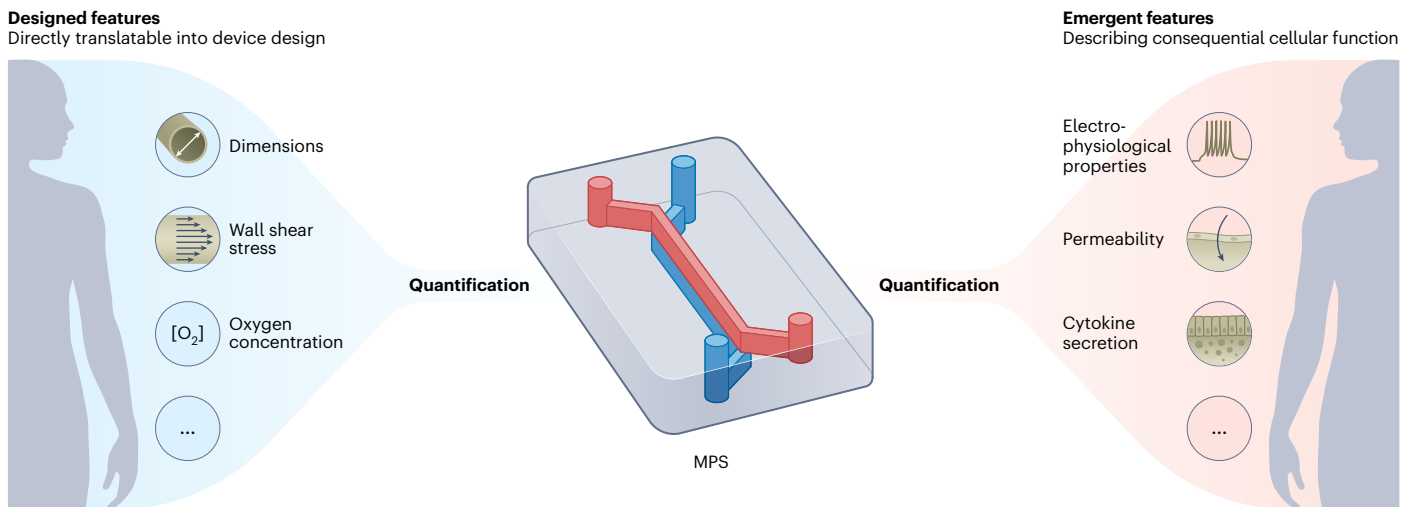## Quantification of physiological features in MPSs

In this section, we describe examples of quantitative modelling of designed and emergent physiological features in MPSs and compare these with values measured in humans (Table 1). We chose to highlight quantifications in MPSs for which the methods and/or values were most similar to quantifications in humans; they can thus be used to assess the relevance of the model and to benchmark certain physiological features in MPSs.

Also, we report physiological features of the healthy state rather than those specifically associated with any pathology. This is to ensure broad relevance in fit-for-purpose applications of MPSs. Although the ultimate goal of MPSs is often modelling disease, these models usually depend on cellular processes that also occur in physiological healthy states. Quantifying healthy features therefore provides a baseline for pathological values, which are often aberrant values of the same physiological features.

Our selection of organs has a developmental focus: to include derivatives of all three germ layers—the mesoderm (heart), endoderm (intestine) and ectoderm (brain)—as well as the blood vessels linking all organs. We discuss a range of MPSs per organ, for which the general design principles and classifications are shown in Figs. 2–5. The majority of MPSs include microfluidics and are thus considered OoCs and referred to as vessel-on-a-chip (VoC), gut-on-a-chip (GoC), heart-on-a-chip (HoC) or brain-on-a-chip (BoC). Our approach and the inclusion criteria used in this Perspective are detailed in Supplementary Discussion 1. We provide descriptions of the designed and emergent physiological features of the four selected organs in Supplementary Fig. 1 and Supplementary Discussion 2 and describe quantified physiological features specific to a single organ in Supplementary Table 1 and Supplementary Discussion 3 and 4.

Designed features

We first describe physiological features that can be directly implemented and controlled as part of the design of the MPS: organ architecture, fluid flow, structural deformation, tissue elasticity and oxygen concentration (Table 1). We focus on how these features have been modelled and measured in MPSs of the vasculature, intestine, heart and brain and emphasize considerations that should be taken into account when comparing in vitro and in vivo measurements. Additionally, in Supplementary Discussion 5 we discuss cell sources and the composition of the cell culture medium for the designed features, which are relevant for any in vitro model system.

Designed features
Directly translatable into device design

Dimensions

Wall shear stress

[O₂] Oxygen concentration

…

Quantification

MPS

Quantification

Emergent features
Describing consequential cellular function

Electro-physiological properties

Permeability

Cytokine secretion

…

Fig. 1 | MPSs can control and monitor physiological features. We distinguish two types of quantifiable physiological feature: designed and emergent. Designed features, such as compartment dimensions, wall shear stress and oxygen concentration, can be controlled via the design of the MPS or through inputs to it. Emergent features, such as electrophysiological properties, permeability and cytokine secretion, describe cellular functions and develop as the combined result of the design features and the responses of the cells in the MPS. Some features may be exclusively designed or emergent and some can be both, depending on the specific model and functional readout.

Organ architecture. Organ function is highly dependent on its organization and architecture. Organoids can recapitulate aspects of tissue architecture accurately, but often suffer from heterogeneity and variability. MPSs provide a means to guide self-organization and to control tissue architecture by using physical confinement or compartmentalization.

Vasculature. To date, no single VoC has been designed to cover the entire range of true vessel diameters. Yet, VoC devices modelling large structures such as arteries and veins and incorporating endothelial and smooth muscle cells exemplify the power of the integration of pre-seeded three-dimensional (3D) tissues with technology for microfabrication and microfluidics. For instance, a biocompatible ink composed of alginate, gelatin methacrylate, sodium alginate and glycidyl-methacrylate silk was used to print tunable hollow microfibres, with dimensions comparable to the in vivo setting, that could be attached to a microfluidic system to provide a physiological microenvironment for cell adhesion and proliferation[7] (Table 1). VoC devices with small diameters are single tubular channels and typically model vessels of 100–500 μm in diameter. Instead, self-assembled vascular networks in hydrogels result in vessels with diameters in the range of 10–500 μm (refs. 8–11). Although these techniques lack flexibility or control of diameters, respectively, laser photoablation allows high-precision patterning of lumenized structures in hydrogels via focused pulsed lasers[12,13].

Intestine. The same laser ablation technique used to design VoCs is also suitable for GoCs and generates perfusable tubular structures with diameters of ~150 μm and containing crypt- and villus-like architectures in a hydrogel[14] (Table 1). Although the dimensions of the tube differ from those of the human intestine, the method shows promise for emulating the intestinal architecture in a controlled manner. Moreover, in most cases, the intention is not to build models that are the exact size of the human intestine; rather, it is to build scaled-down in vitro model systems, with the most relevant dimensions being the diameter-to-length ratio of the intestinal tube and the diameter-to-height ratio or diameter-to-depth ratio of the villus and crypt, respectively.

Heart. The heart consists of multiple open chambers with specific geometries that are essential for building up the internal pressure necessary to pump blood through the body. Most HoC devices do not model the entire geometry of the heart or its individual chambers; rather, they generate functional cardiac muscle tissues. Some HoC devices have modelled the entire architecture or individual heart chambers either at a macroscale or by scaling down to the microtissue level. Steps towards macroscale heart chamber geometries have been made by creating ellipsoidal nanofibrous scaffolds, compatible with microfluidic systems and the application of exogenous pressure, seeded with ventricular cardiomyocytes derived from human induced pluripotent stem cells[15] (hiPSCs). Ultimately, the chamber geometry and volume are crucial determinants of the forces generated on and by the cardiomyocytes in the engineered chambers. A microscale multi-chamber microfluidic device has been developed with integrated sensors for measuring the pressure within the chambers. This pressure was induced by pneumatic membranes creating fluid flow in a closed loop covered with human umbilical vein endothelial cells, with four solenoid valves ensuring unidirectional flow through the four chambers[16].

Brain. The most distinctive architectural feature of the brain is its spatial organization into different regions and the specific layering of cells within these regions. BoC models have been developed to mimic connections between and within different mature brain regions by linking compartmentalized co-cultures containing different region-specific neuronal cell types[17,18] (Table 1). However, recapitulating the architecture of the six neuronal layers of the cortex requires self-organization (which suffers from inherent variability) or the compartmentalization of different cell types. This has been achieved in a BoC model using a polydimethylsiloxane (PDMS) stencil to create separate microchambers for seeding different neuronal cell types[19]. Although this BoC model does not completely mimic cortex development in vivo, the layered cellular architecture of the cortex can be recreated. In the future, combining the approaches for brain region specification and cellular layering may enable the recreation of a full (micro)cortex.

Fluid flow. Organs depend on fluid flow to receive nutrients and immune protection and to dispose of waste products. In this subsection we discuss luminal fluid flow and in Supplementary Discussion 3 and Supplementary Table 1 we discuss interstitial flow (for VoC models).

Table 1 | Quantification of designed and emergent physiological features in MPSs and humans

Category	Organ	Feature	MPS method	MPS quantification	Human quantification	Reference (MPS)	Reference (human)
Designed							
Organ architecture	Vessel	Tube diameter	Laser ablation	10–500 µm	Arteries: 0.03–2.5 cm	12	
			3D bioprinting	700–1,000 µm	Arterioles: 10–300 µm; Capillaries: 5–10 µm; Venules: 8–100 µm; Veins: 0.01–2.00 cm	7,150	149
		Tube dimensions	Laser ablation	Diameter: 150 µm Length: 1,200 µm DLR: 0.125	Diameter: 2.5 cm (SI); 4.8 cm (LI) Length: 300 cm (SI); 110–190 cm (LI) DLR: 0.008 (SI); 0.025–0.044 (LI)	14	151
	Intestine	Crypt–villus dimensions	Laser ablation	Crypt: Diameter: 50–75 µm Depth: 170 µm DDR: 0.29–0.44	Crypt SI: Diameter: 50 µm Depth: 132–219 µm DDR: 0.23–0.38 Villus SI: Diameter: 132–165 µm Height: 273–720 µm DHR: 0.18–0.60	14	152–154
	Heart	Ventricular chamber volume	Nanofibrous scaffold	500 µl	147 ml	15	155
	Brain	Regional connections	Compartmentalized system	Connection between the dentate gyrus and CA3 neurons within the hippocampus	Separation of functional and structural neurons between and within brain regions	17	156
		Cortical layering	Compartmentalized system	Two cortical layers	Six cortical layers	19	157
Fluid flow	Vessel	Wall shear stress	Various pump systems	Arteries: 1.2–1.5 Pa Arterioles: 0.42 Pa Capillaries/venules: 0.03–0.72 Pa Veins: 1 Pa	Arteries: 2.23 Pa Arterioles: 6–14 Pa Capillaries: 1.2 Pa Venules: 0.3–1.0 Pa Veins: 0.1–0.6 Pa	10,20–23	158,159
		Circumferential strain	Syringe pump	4–10%	5–10%	27	160,161
	Intestine	Wall shear stress	Pressure-driven flow	0.6–6.0 mPa	~0.2–8.0 mPa	24	24–26,162
			Syringe pump	2 mPa		26	
	Brain	Cerebral spinal fluid flow	Miniature osmotic pump	0.15 µl min⁻¹	0.02–3.00 ml min⁻¹ depending on brain structure	163	164
Structural deformation	Intestine	Peristalsis	Vacuum chambers lining microchannel	Deformation: 0–30% Frequency: 0.15 Hz	Deformation: 7.2–27.4% (SI) Frequency: 0–10 Hz (SI); 0.06–0.70 mHz (5–61 d⁻¹) (LI)	24	162,165
			Vacuum chambers lining microchannel	Deformation: 5% Frequency: 0.15 Hz		26	
	Heart	Afterload	External magnets	0.61–5.40 mN mm⁻²	8.31 mN mm⁻² (human modelling)	29	29
	Vessel		Tunable synthetic hydrogel	1–6 kPa	Arteries: 50–150 kPa Venous: 3–50 kPa (mouse)	40	30
Tissue elasticity	Intestine	ECM elasticity	Hydrogel	0.75 kPa	SI: 0.6–2.6 kPa LI: 0.9 kPa	14	32
			Chemically crosslinked hydrogel	9.46 kPa		38	
	Heart		Varying the acrylamide/bis composition	1, 13 and 90 kPa (soft, normal and stiff, respectively)	Foetal: ~1 kPa Adult: ~13 kPa	39	166
	Brain		Brain tissue-derived ECM	0.1 kPa	0.4 kPa	37	33
Oxygen concentration	Vessel	Oxygen concentration	Oxygen scavenging channel	1–5%	1–13%	49	167
	Intestine		Integrated oxygen sensors	~0.3–1.5% (gradient outlet–inlet epithelium channel)	Intestinal lumen: ~4–5% (SI); ~0.4–1.5% (LI)	48	168
	Heart		Hypoxic incubator	1, 5 and 21%	5–10%	47	169
	Brain		Hypoxic incubator	5%	1–5%	46	170

Table 1 (continued) | Quantification of designed and emergent physiological features in MPSs and humans

Category	Organ	Feature	MPS method	MPS quantification	Human quantification	Reference (MPS)	Reference (human)
Emergent							
Cell type diversity	Vessel	Cell type diversity	scRNA-seq	-	ECs, SMCs, pericytes, perivascular fibroblasts and macrophages (heterogeneous between tissues and along the arteriovenous axis)	–	171
	Intestine	Epithelial cell type diversity	scRNA-seq	61% ent; 22.7% PC like; 9.1% TA/SC; 1.8% EEC; 1.4% gob	Ileum: 70–75% ent; 10–11% prog; 5% gob; 4–5% TA/SC; 1–2% PC; 0–1% EEC Colon: 35% prog; 20–22% gob; 15% ent; 12–14% TA; 8–10% PC; 3–4% SC; 0–1% EEC	50	172
	Heart	Cell type diversity	scRNA-seq	-	30% cardiomyocytes; 24% fibroblasts; 17% mural cells; 12% ECs; 10% immune cells	–	173,174
	Brain	Cell type diversity	scRNA-seq	Early neuronal cell types from rostral and caudal neural tube	Ten major cell types; highly heterogenous between brain regions	51	175–178
Cell localization and cell–cell interactions	Vessel	Astrocyte coverage of endothelial layer	IF co-localization	9%	100% (rat)	58	179
	Vessel	Pericyte coverage of endothelial layer	IF co-localization	16%	10–70% average all tissues; 30% BBB (rat)	58	179,180
	Intestine	Epithelial cell type localization along crypt-villus axis	IF (fluorescence intensity along crypt-villus axis)	Score from 0 (base) to 1.0 (top): proliferative cells=0–0.5; differentiated cells=0.5–1.0	Score from −0.2 (base) to 1.0 (top): SC=−0.2–0.2; gob=−0.1–0.3; EEC=−0.1–0.3; ent=0.1–0.9	55	56
	Intestine	Regional specification	WNT gradient via microfluidics	Regional development along rostral-caudal axis	Regional development along the rostral–caudal axis	51,57	181
	Brain	Synapse density	IF	2.2–2.6×10^3 synapses per μm^2	8.6–12.9×10^8 synapses per mm^3	59	182
	Brain	Neurotransmitter release and uptake	In-chip electrochemical sensors	1min timescale	Millisecond timescale (mouse/rat)	60	61,183
Inflammatory responses	Vessel	Cytokine secretion	Luminex IL-6	$0.3\,ng\,ml^{-1}$	0.1–$305\,ng\,ml^{-1}$	66	184
	Intestine	Cytokine secretion	Multiplex assay (LPS, IFNγ and TPCA-1 stimulated)	Percentage of inhibition (apical/basal): IL-8=60%/70%; CCL-20=55%/70%; CXCL10=10%/50%	-	67	
	Brain	Cytokine secretion	Membrane-based antibody array	Upregulation of inflammatory cytokines	Upregulation of inflammatory cytokines	68	185
Barrier integrity	Vessel	Permeability of the endothelial layer	Leakage assay (20kDa)	$3\times10^{-6}\,cm\,s^{-1}$	$2.4\times10^{-7}\,cm\,s^{-1}$ (rat)	72	186
	Vessel	Permeability of the endothelial layer	Leakage assay (70kDa)	$4\times10^{-7}\,cm\,s^{-1}$	$1.5\times10^{-7}\,cm\,s^{-1}$ (rat)	70	186
	Intestine	Permeability of the epithelial layer	Fluorescent tracer leakage (4.4kDa FD)	P_{app}: $7.12\times10^{-6}\,cm\,s^{-1}$	0.11–$0.12\times10^{-6}\,cm\,s^{-1}$ (SI); 0.05–$0.10\times10^{-6}\,cm\,s^{-1}$ (LI)	71	187
	Intestine	Permeability of the epithelial layer	Rhodamine 123 permeability	Influx: $5\times10^{-6}\,cm\,s^{-1}$ Efflux: $1\times10^{-6}\,cm\,s^{-1}$	-	74	
	Intestine	Permeability of the epithelial layer	LC-MS (caffeine and atenolol)	Caffeine: $34.5\times10^{-4}\,cm\,s^{-1}$ Atenolol: $3.8\times10^{-4}\,cm\,s^{-1}$	Caffeine: $2.93\times10^{-4}\,cm\,s^{-1}$ Atenolol: $0.2\times10^{-4}\,cm\,s^{-1}$	75	75
Electrical signalling	Heart	Resting membrane potential	Patch clamp	−97mV		188	
	Heart	Resting membrane potential	Impaling electrode measurement	−57mV	-90mV	81	189
	Heart	Action potential amplitude	Impaling electrode measurement	97±2mV	102–110mV	81	189
	Heart	Conduction velocity	Voltage-sensitive dye and optical mapping	$47.4\pm12.4\,cm\,s^{-1}$	30–$100\,cm\,s^{-1}$	77	189
	Brain	Electrical frequency	MEA	0.2–3.0Hz	0.05–500Hz oscillations	84	190
Tissue renewal	Vessel	Angiogenesis	Imaging	$16\,\mu m\,h^{-1}$	-	88	–
	Intestine	Epithelial turnover rate	EdU pulse-chase (12h pulse; 10d chase)	4d for full turnover	3.48d (average EGI epithelium)	14	162,191
	Intestine	Epithelial migration speed (crypt to villus)	EdU pulse-chase (24h pulse; 96h chase)	$40\,\mu m\,d^{-1}$	38–$63\,\mu m\,d^{-1}$ (SI; neonatal rat); $216/143\,\mu m\,d^{-1}$ (duodenum/ileum; mouse)	38	192,193

Data were included on the basis of the criteria stated in Supplementary Discussion 1. An en dash indicates that data were not available. CCL, C–C-motif chemokine ligand; CXCL, C–X–C-motif chemokine ligand; DDR, diameter-to-depth ratio; DHR, diameter-to-height ratio; DLR, diameter-to-length ratio; EC, endothelial cell; EEC, enteroendocrine cell; EGI, entire gastrointestinal; ent, enterocyte; FD, fluorescein isothiocyanate–dextran; gob, goblet cell; IF, immunofluorescence; IFNγ, interferon-γ; LC-MS, liquid chromatography–mass spectrometry; LI, large intestine; LPS, lipopolysaccharide; P_{app}, apparent permeability; PC, Paneth cell; prog, progenitor cell; SC, stem cell; scRNA-seq, single-cell RNA sequencing; SI, small intestine; SMC, smooth muscle cell; TA, transit-amplifying cell.
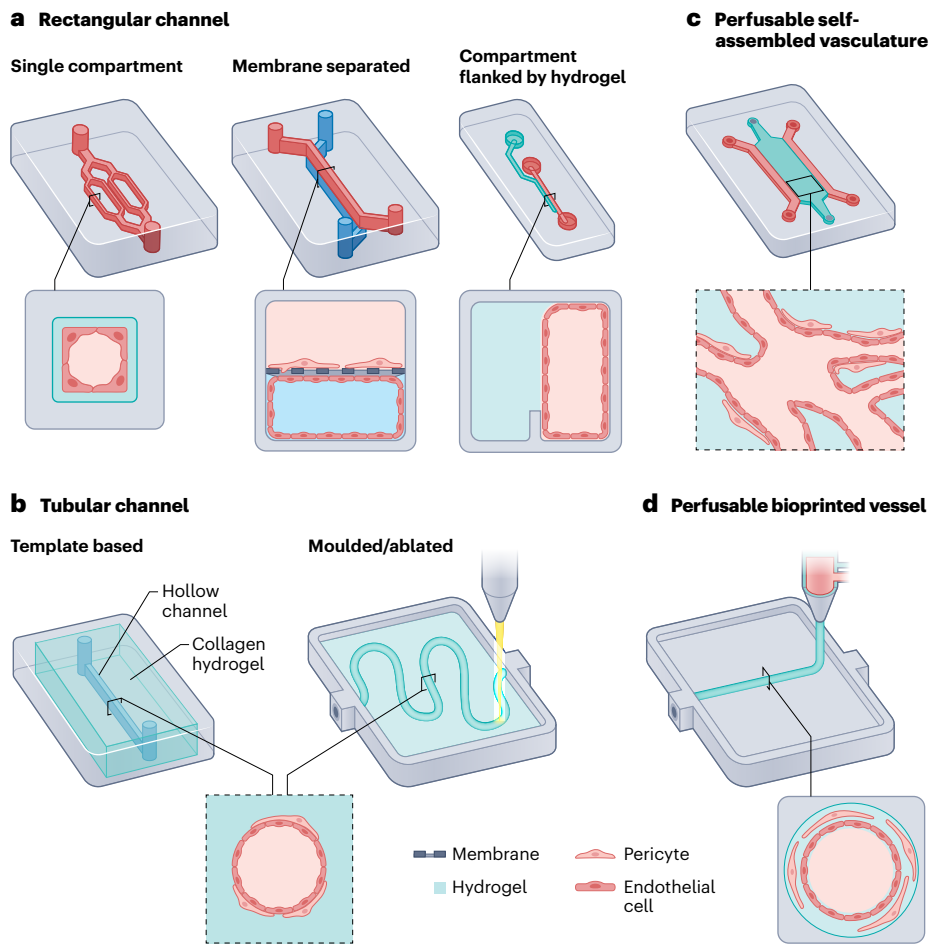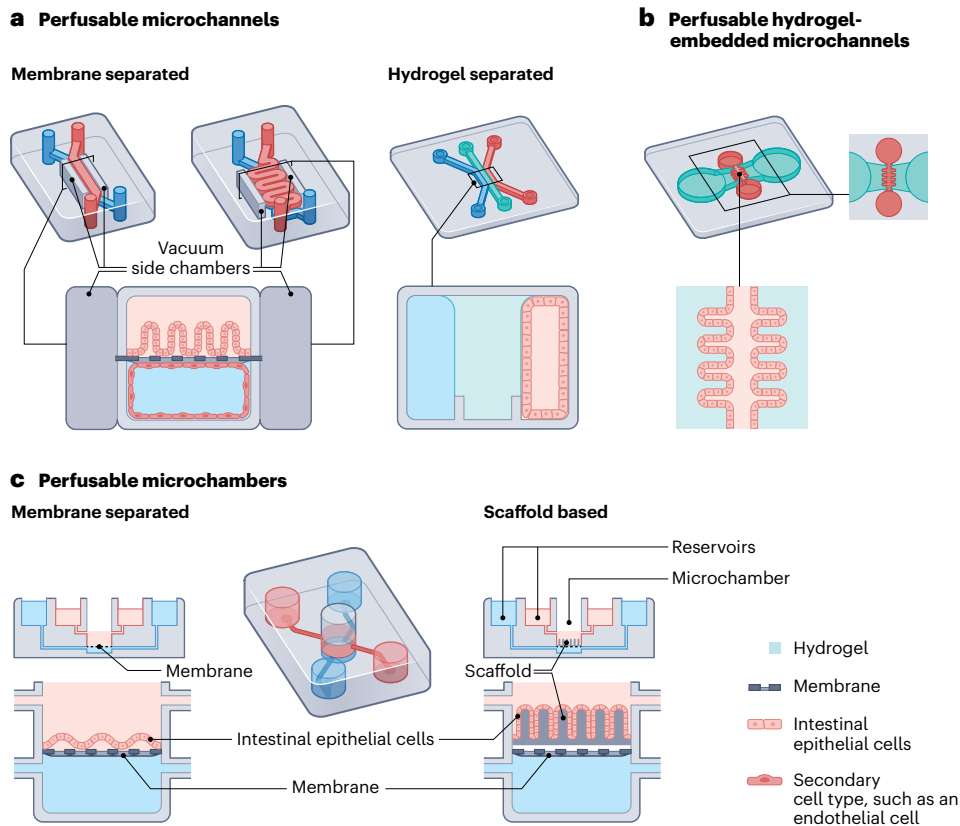
Fig. 2 | Design principles of MPSs of the human vasculature. a, Left, a single patterned channel, usually made with PDMS or an agarose gelatin hydrogel, is widely used for monocultures of endothelial cells. Middle, two aligned channels separated by a porous membrane. Unidirectional pressure-driven fluid flow can be introduced in both channels. The device is made of PDMS and coated with a thin hydrogel layer. Cells can be cultured in both channels. The top channel is usually seeded with tissue-specific cell types (such as astrocytes, neurons, lung epithelium or intestinal epithelium) and the bottom channel is seeded with endothelial cells. Right, a two-channel device designed for use with gravitational bidirectional flow. One channel is used to seed endothelial cells and is flanked by a hydrogel-filled channel separated using a phase guide. Tissue-specific cells can be seeded in the hydrogel channel. **b**, Left, tubular channels that use templating are made by removing or replacing a structure within a hydrogel via needle removal or by using differences in fluid viscosity (as with viscous finger patterning). The tubular structure can be seeded with cells. Right, moulding or laser ablation can be used to pattern tubular structures within hydrogels. **c**, MPSs leveraging the ability of endothelial cells to self-organize into vascular networks. To enable the development of a 3D vascular network, endothelial cells are usually mixed with mural cells and the mixture is seeded in a hydrogel channel. Perfusion of the hydrogel channel is enabled by flanking it with channels filled with media. **d**, Perfusable cell-laden hydrogels within a predetermined structure can be bioprinted, seeded with cells and connected to a microfluidic setup. Panels adapted with permission from: **a**(left), ref. 70, Springer Nature Limited; **a**(right), ref. 72, Springer Nature Limited.

Luminal fluid flow exerts mechanical forces on cells in a tubular wall and is proportional to the local flow rate, local lumen geometry and viscosity of the fluid. The resulting wall shear stress is sensed by the cells and transduced into biological responses, such as altered permeability and cellular remodelling. In the vasculature, large internal pressures in combination with wall elasticity result in circumferential strain as an additional force on these cells.

Several microfluidic solutions allow for the establishment of physiologically relevant fluid flow in OoCs. The highest flow rates in the human body are in the arteries and these can best be replicated using peristaltic piezoelectric pumps as they can produce pulsatile flow with high flow rates because of their inherent high-frequency output. This was shown experimentally by using a piezoelectric braille pin system to actuate a peristaltic pump that induced flow rates (30 mm s^{-1}) corresponding to up to 1.2 Pa of wall shear stress on endothelial cell cultures[20] (Table 1). As seen in vivo, endothelial cells align and elongate with increasing flow rates. Pneumatic systems are also used because of their high force output, which supports high flow rates. For example,

the arteriovenous specification of hiPSC-derived endothelial cells, as quantified by the expression of arterial and venous markers, could be controlled in a microfluidic setup with six parallel cell culture chambers with shear stresses of up to 1.5 Pa (ref. 21). Arteriole-like flow profiles and flow rates can also be achieved in various microfluidic systems, as long as they have pulsatile flow options. For example, a microfluidic heart-like valve using a pressure system could reproduce pulsatile flow accurately[22]. However, 0.42 Pa was the maximum achievable wall shear stress and this amount is lower than that in vivo (Table 1). Capillaries and venules both require low flow rates with laminar profiles inside a channel of just a few micrometres in diameter. These requirements can be fulfilled in at least two ways: via hydrostatic pressure, where low flow rates can be approximated by the addition of different volumes of media in the microfluidic reservoirs of the device[10] (however, a disadvantage of this approach is the varying flow rate, and thus wall shear stress, over time); and via pressure-driven pumps, which are preferred for modelling veins because they can reproduce a steady non-pulsatile pattern with a high flow rate (this was exemplified in a

Fig. 3 | Design principles of MPSs of the human intestine. a, Left, two aligned channels separated by a porous membrane. The channels can either be linear or curved. Unidirectional pressure-driven fluid flow can be introduced in both channels. The device is typically made of PDMS and coated with a thin hydrogel layer. Cells can be cultured in both channels. The top channel is usually seeded with intestinal epithelium and the bottom channel with endothelial cells. Two smaller vacuum chambers are placed parallel to the microfluidic channels to pressurize and stretch the membrane and to recapitulate peristaltic movement. Right, two aligned channels separated by a hydrogel layer. Cells can be cultured in all three compartments. Bidirectional gravitational fluid flow can be introduced in both channels. The channels are coated with a thin layer of hydrogel. **b**, A tubular microchannel embedded in a hydrogel with villus–crypt architecture, created via laser ablation. The device contains two separate media compartments—one for perfusion of the microchannel lumen and the other for perfusion of the hydrogel surrounding the microchannel—to create a gradient through the hydrogel. Cells can be grown in the microchannel or in the hydrogel. Unidirectional fluid flow (via a syringe pump) can be introduced in the microchannel. **c**, Two microchambers separated by a porous membrane. The top compartment is usually used for cell culture. Left, pressure-driven unidirectional flow (via a peristaltic pump) can be introduced in both chambers. Right, a scaffold with villus–crypt architecture can be located on the membrane. Gravitational bidirectional flow can be introduced in both chambers. Panels adapted with permission from: **a** (left), ref. 26 under a Creative Commons license CC BY 4.0; **b**, ref. 14, Springer Nature Limited; **c** (right), ref. 74, Springer Nature Limited.

study of the alignment of human umbilical vein endothelial cells upon recirculation flow at shear stresses of up to 1 Pa[23].

Pressure-driven pumps are also commonly used to model luminal fluid flow in GoC models. One of the first GoC devices used this technique to expose the cells to a physiologically relevant wall shear stress, ranging from 0.6–6.0 mPa, depending on the flow rate[24] (Table 1). To simplify device design, most VoC and GoC devices model the organ as a straight cylindrical or rectangular microchannel, thereby neglecting the irregular turns that can profoundly impact flow profiles[25]. In fact, a GoC model that integrated a nonlinear asymmetric flow profile allowed for a more precise representation of in vivo intestinal flow[26] (Table 1).

Importantly, although various technologies now support the integration of physiologically relevant flow profiles in in vitro models, it is essential to verify the biological relevance of the resultant forces for the resident cells. Wall shear stress, instead of absolute flow rate, provides a single measure that can be used to compare OoCs with human physiology because it considers channel geometry, fluid properties and flow parameters. However, accurately modelling circumferential strain remains technically difficult, yet advances such as the use of a template-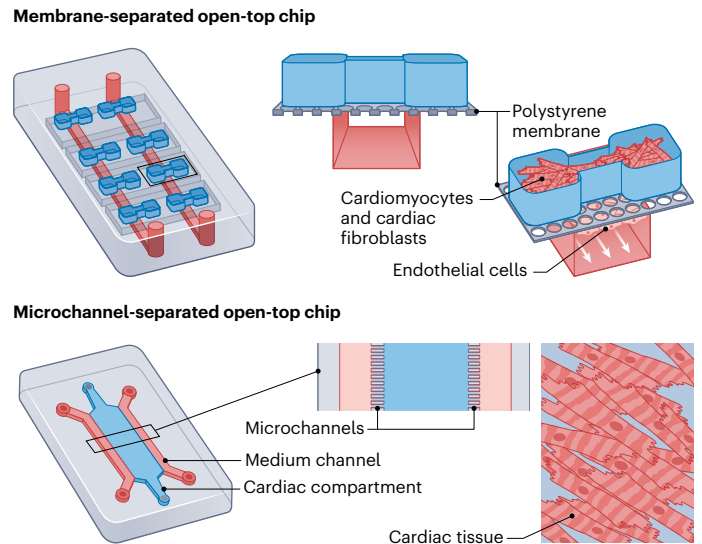based tubular VoC model coupled to a syringe pump have allowed for the recapitulation of physiological values (Table 1)[27]. Future modelling of circumferential strain could be further improved by using new piezoelectric materials (as discussed in the section 'Technical advances for the quantification of physiological features').

Structural deformation. Many organs contain muscle cells that structurally deform the tissue. MPSs exploit several principles to induce these types of structural deformation and strain on cells. For instance, several GoC models mimic peristalsis by including vacuum chambers flanking the microchannels so as to induce rhythmic membrane deformation through cyclic suction. This approach can generate physiologically relevant deformations of 0–30% at a frequency of 0.15 Hz[24] (Table 1). One recent GoC displayed a nonlinear curved channel in which the flanking vacuum chambers induced multiaxial cellular deformation rather than the biaxial deformation induced by linear microchannels[26] (Table 1). This setup better reflects complex human intestinal movement at both the macroscopic level and the microscopic level (in particular, villus motility). In these GoC models, the device design replaces muscle cell function; hence, they do not need to incorporate muscle cells.
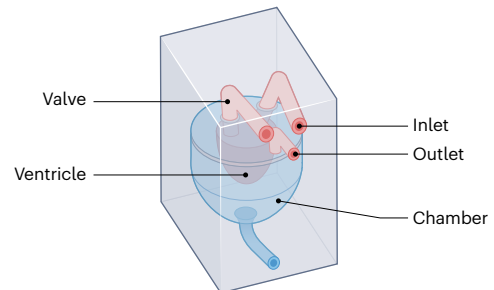
a Cardiac tissue on cantilevers

Standing model   Hanging model

Biowire model
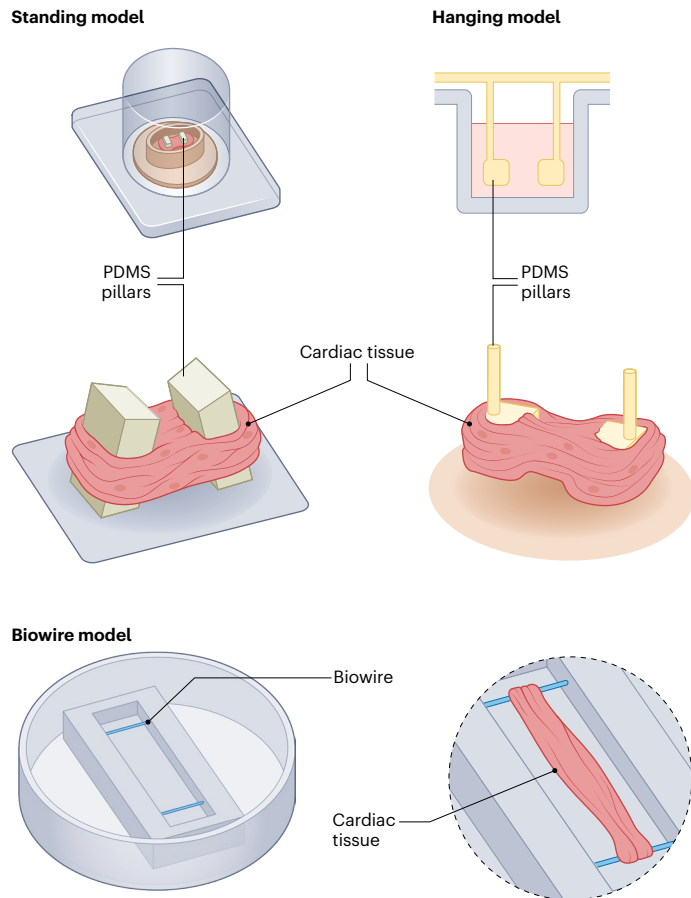
b Compartmentalized chip defined by cardiac tissue shape

Membrane-separated open-top chip

Microchannel-separated open-top chip

c Perfused heart chamber model

Fig. 4 | Design principles of MPSs of the human heart. a, Top left, standing rectangular micropillars, typically made of PDMS, that fit into 96-well plates. Top right, hanging cylindrical pillars, also typically made of PDMS, in a rack of four pairs (only one pair is shown) that fit into 24-well plates. Bottom, patterned polystyrene sheets (Biowire), where 3D cardiac tissue is anchored to two horizontal wires within a chamber with two carbon electrodes (not shown) for electrical stimulation. b, Top, open-top compartment with a dog bone-shaped cardiac tissue on top, separated by a porous polystyrene membrane.

The bottom channel is perfusable and can be used as an endothelial cell compartment. Bottom, a channel confining cardiac tissue, with side microchannels stimulating the diffusion of nutrients from the flanking media channels. c, A polycaprolactone or gelatin-based heart chamber scaffold with inlet and outlet channels, as well as a catheter with a valve, for pressure and volume measurements. Panels adapted with permission from: a(bottom), ref. 194, Elsevier; b(bottom), ref. 195, Springer Nature Limited; c, ref. 15, Springer Nature Limited.

The design of MPSs of the heart should ensure stimulation (and, optionally, control) of the contraction of the cardiac muscle cells. In this way, the design allows modelling of specific states of the heart, such as cyclic stretch or afterload (a period of systolic contraction when cardiac cells are exposed to increased strain, so that they can pump against the arterial pressure). Cantilever-based engineered heart tissues mimic afterload by organizing the cardiac tissues around pillars or micropoles on a flexible membrane so that strain can be increased pneumatically[28]. Alternatively, afterload can also be modified dynamically in engineered heart tissues that contain small magnets controlled by a piezoelectric stage[29]. Piezoelectric materials and ionic polymer–metal composites (IPMCs) can also provide precise control of actuation and stimulation in MPSs (as discussed in the section 'Technical advances for the quantification of physiological features').

Tissue elasticity. Tissue elasticity influences many cellular responses and is often altered during disease as a result of fibrosis. Most cell types react to changes in the mechanical properties of the extracellular matrix (ECM) by converting mechanical cues into biological responses. Changes in ECM elasticity can cause pathological angiogenesis[30],

cardiomyocyte maturation (which may induce heart failure[31]), expansion of intestinal stem cells (which may favour cancer progression[32]) and alteration of neuronal differentiation, wiring and plasticity[33].

Tissue elasticity, which is described by the elastic modulus, can vary in the human body from <1 kPa for some soft tissues (such as the brain) to >10 kPa for muscle tissues[33]. Conventional in vitro experiments are often carried out on glass or plastic, which are far stiffer (in the GPa range). Commonly used alternatives are soft natural hydrogels such as collagen, fibrin or Matrigel (<1 kPa)[34,35]. Many MPSs are composed of stiff materials, such as PDMS (0.8–4.0 MPa)[36] coated with a thin layer of ECM. Because these substrates do not accurately reflect the elasticity of soft tissue in vivo, natural hydrogels have been used to generate softer scaffolds for these systems. One GoC model used laser ablation to create a microchannel in polymerized hydrogel containing neutralized collagen and Matrigel, which resulted in an elastic modulus of 0.75 kPa[14] (Table 1). This approach led to the generation of a perfusable microchannel containing villus–crypt architecture. Another way to model soft tissues is to use decellularized human tissue-derived ECM, as was shown for a microfluidic BoC system[37] with hiPSC-derived brain organoids that led to physiologically relevant elasticity, improved cortical layering and electrophysiological function. The obvious
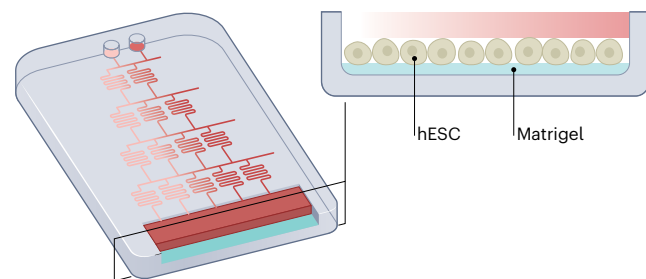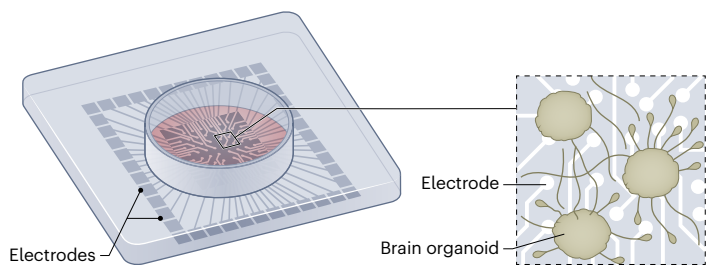
a Compartmentalized chip
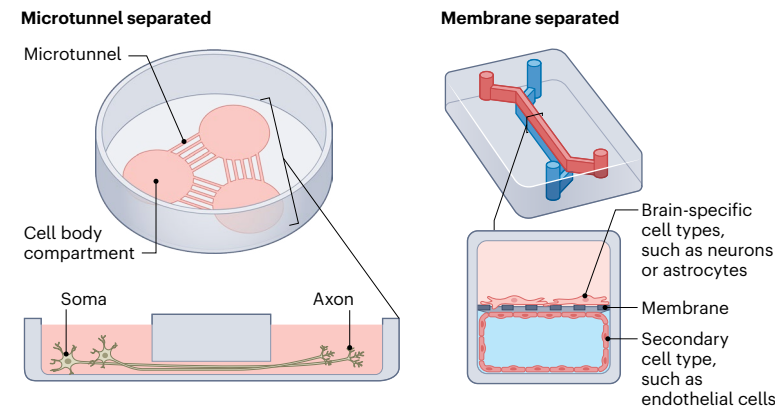
b Perfused tissue chamber
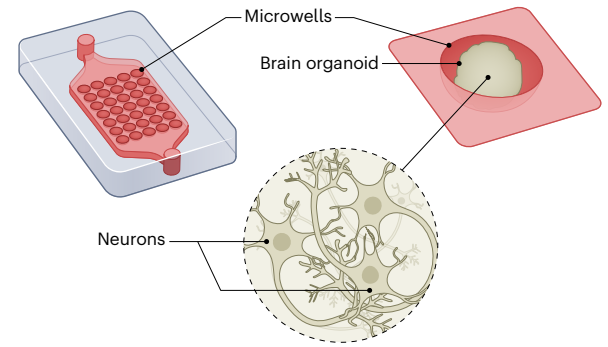
c Gradient-inducing chip

d Multielectrode array integrated in a chip

Fig. 5 | Design principles of MPSs of the human brain. a, Left, specific cell–cell interactions can be modelled via devices with multiple cell culture compartments connected by microtunnels to physically separate the cell bodies of different cell types (the cells are unable to migrate) while allowing their protrusions to extend into a nearby compartment. Right, two aligned channels separated by a porous membrane. Unidirectional pressure-driven fluid flow can be introduced in both channels. The device is made from PDMS and is coated with a thin hydrogel layer. Cells can be cultured in both channels. The top channel is usually seeded with tissue-specific cell types (such as astrocytes or neurons) and the bottom channel is seeded with endothelial cells. **b**, A perfused tissue chamber containing microwells to enable the culture of brain organoids in the presence of interstitial flow. **c**, An MPS with a linear growth factor gradient established over the cell culture area via the diffusive mixing of two inlet media. hESC, human embryonic stem cell. **d**, System with an integrated MEA for measuring the electrophysiological activity of neurons (either single neurons or neuron organoids). Panels adapted with permission from: **a** (right), ref. 46, Springer Nature Limited; **c**, ref. 51, Springer Nature America, Inc.

drawback is the need for human tissue for ECM derivation (however, porcine-derived ECM may also be suitable).

Most other tissues, including certain parts of the intestine, have tissue elasticities >1 kPa and thus require modified hydrogels or other hydrogel chemistries. Moreover, because natural hydrogels are too soft to generate standing structures, for some applications stiffer materials are necessary. One approach is to crosslink natural hydrogels, as exemplified by a non-perfused scaffold-guided intestinal tissue model that used chemically crosslinked collagen to increase the hydrogel elasticity to 9.46 kPa (ref. 38). This allowed for moulding of the hydrogel (via a PDMS stamp) into standing micropillars and microwells that led to recapitulation of the architecture of the human small intestine. Alternatively, tunable synthetic hydrogels can be used. Notably, these can be made to mimic the stiffened substrate of the heart during foetal states (1 kPa), normal states (13 kPa) and diseased states (90 kPa)[39] and to model angiogenic sprouting with physiologically relevant elasticity (1–6 kPa; Table 1)[40].

Therefore, the need to achieve a balance between ease of use and biological compatibility constrains tissue elasticity in MPSs. This could be resolved via recently developed materials, such as soft thermoplastic elastomers (TPEs) and chemically enhanced versions of PDMS, which allow for the modulation of elasticity in 3D cultures. Also, these materials can be used in standard fabrication methods, such as injection moulding, hot embossing, 3D printing and micromachining (Table 1)[41–43]. In addition, smart materials responsive to changes in pH,

ion concentration, temperature or electric field[44,45] could be used to control the mechanical properties of the tissue more accurately.

Oxygen concentration. The vasculature, intestine and heart have unique oxygen profiles with steep gradients from one region to another. Most MPSs are made of gas-permeable polymers such as PDMS and are cultured in standard incubators with supraphysiological oxygen conditions (21% O_2). To recapitulate the in vivo oxygen concentration more closely, the most straightforward technique is to place the PDMS device in an anaerobic incubator. For example, a device integrating a BoC and a VoC to model the blood–brain barrier (BBB) under hypoxic conditions (5% O_2) led to enhancements in the formation of the barrier, resulting in higher impedance between microfluidic chambers and selective shuttling of drugs and antibodies[46]. Similarly, HoC devices containing human 3D cardiac tissues can be placed in environmental chambers with varying oxygen concentrations (1, 5 and 21%)[47] to study hypoxia, which is crucial to mimic myocardial infarction and the fibrosis that follows heart damage. Although no differences in viability were seen across the different levels of oxygen, the myofibroblast marker α-smooth muscle actin was upregulated and the contractile function was impaired[47].

Active perfusion of a system in an oxygen-controlled environment can also be used to create aerobic and anaerobic compartments within the same device. Such a system is well suited for achieving physiologically relevant oxygen concentrations in GoC models. For example,

perfusion of a PDMS-based GoC in an anaerobic chamber with deoxygenated medium in the top channel and oxygenated medium in the bottom channel[48] created an oxygen gradient that ensured the survival of the anaerobic microorganisms in the top channel and the human epithelial cell layer growing on the membrane separating the top and bottom channels. Integrated sensors, which allowed for real-time measurements of oxygen tension, showed that physiologically relevant oxygen concentrations were reached (<0.3% in the epithelial channel and ~10% in the endothelial channel), which supported the maintenance of complex human microbial cultures for 5 d (Table 1). The same system can be used to create oxygen gradients along the length of the intestinal epithelial channel. A more subtle solution for creating physiologically relevant oxygen concentrations in MPSs was shown in a VoC where temporal and spatial regulation of the distribution of oxygen was achieved in a hydrogel culture chamber by using an oxygen scavenger in the adjacent microfluidic channels[49]. This resulted in controlled and easily adjustable oxygen concentrations within the physiological range of 1–5% and allowed the study of angiogenic bias to hypoxic environments (Table 1). For MPSs to approximate physiologically relevant oxygen concentrations without using an anaerobic chamber or oxygen scavengers, polymers with lower permeability to oxygen may be needed (see 'Technical advances for the quantification of physiological features').

Emergent features

In this section, we describe physiological features that develop as a consequence of device design, the microenvironment and the cell type and that can be measured as a system readout (for example, cell type diversity, cell localization and cell–cell interactions, inflammatory responses, barrier integrity, electrical signalling and tissue renewal; Table 1). We focus on how these features have been modelled and measured quantitatively in MPSs of the vasculature, intestine, heart and brain and emphasize factors that should be considered when comparing in vitro and in vivo measurements. The quantified emergent features that are specific to a single organ are described in Supplementary Discussion 4 and Supplementary Table 1 and include cellular contraction (for HoC models), microbiome diversity, immune cell infiltration, mucus layer thickness and digestion and absorption (for GoC models), neuron-specific morphological features that support electrical signalling (for BoC models) and monocyte speed (for VoC models).

Cell-type diversity. Proper organ function relies on the presence of diverse and often organ-specific cell types. For most MPSs, only seeding compositions are quantified to assess cell type ratios; however, these do not necessarily reflect the cell type diversity at the time that functional readouts are made because cell diversity will be influenced by the microenvironment and by whether the cells proliferate differentially. Quantification of cell type diversity at the time of readout is therefore essential for comparing different in vitro systems and for assessing their in vivo relevance.

For most MPSs, cell types are quantified by immunofluorescence staining, which provides insight into both cell type diversity and localization. However, immunofluorescence is limited by the use of established markers and makes quantification difficult. Alternatively, single-cell RNA sequencing can be used to quantify cell type diversity in an unbiased manner and to compare gene expression profiles with human equivalents, as was shown for an hiPSC-derived GoC system[50] (Table 1). Single-cell RNA sequencing has also been used to profile brain organoid tissue and region-specific neurons in a BoC (albeit only for early-stage progenitors and neurons)[51] (Table 1) and to investigate the effect of different flow profiles[52] and endothelial autophagy in angiogenic sprouts[53] in VoC systems, but not yet to assess cell type diversity in VoCs and HoCs. Current VoC systems have not yet modelled the full complexity of the vascular tree and most HoC devices use a combination of cardiomyocytes and fibroblasts, typically in a four-to-one ratio.

Certain HoC devices have been fabricated to facilitate specific cellular niches; for example, a microfluidic chip incorporating a bilayer membrane allowed for the separation and transmigration of endothelial cells to the cardiac compartment[54]. However, for many systems, including BoC, VoC and HoC models, high-resolution measurements of the heterogeneity of human cell types and comparisons with in vivo data have yet to be carried out.

Cell localization and cell–cell interactions. Tissue functionality depends on cell type diversity and the location of cells within a tissue and their interaction with each other. The spatial organization and co-localization of different cell types can provide insight into tissue-specific microenvironments and intercellular communication. These features have been quantified in different MPSs via immunofluorescence staining and microscopy.

A non-perfused intestinal tissue model that used a scaffold to create growth factor gradients exemplified the possibility of controlling and quantifying the spatial organization of intestinal epithelial subtypes along the crypt–villus axis[55]. Specifically, immunostaining was used to distinguish proliferative and differentiated epithelial populations and to quantify their abundance and location along the crypt–villus length. The epithelial subtype distribution in the developing human intestine was reported using a similar approach, by scoring the position along the crypt–villus[56]. Hence, this approach allows for comparison with the human intestine and can be used in GoC models independent of whether the tissue is scaffold guided or self-organized (Table 1). Similarly, the spatial organization of neurons was modelled in BoC systems that incorporated microfluidics to recapitulate growth factor gradients along the rostral–caudal axis of the neural tube[51,57]. This technique allowed for microfluidic-controlled stem cell differentiation and regionalization and resulted in spatially organized neuronal subpopulations resembling those seen during the development of the human brain.

Besides using fluorescence readouts to quantify cell localization, fluorescence also allows for study of the co-localization of different cell types as an indication of cell–cell interactions. This was shown for a self-assembling model of the BBB by quantifying the coverage of the endothelial abluminal side by both pericytes and astrocytes through maximum projection images of confocal z stacks[58]. Similarly, the formation of synaptic connections in neuronal cells has been quantified in a BoC with two lateral chambers connected by a central channel through an array of microgrooves[59]. This allowed for controlled quantification of dopaminergic synapses in the central channel via fluorescent labelling of pre-synaptic and post-synaptic markers. However, quantification was done on a z-projection of an area in a 3D chip; it is therefore challenging to directly compare with numbers in the human cortex, which were quantified as the number of synapses per volume (Table 1). A BoC system that applied high-temporal-resolution electroanalysis of neurotransmitter homeostasis demonstrated a more functional method of quantifying cell–cell interactions in neuronal synapses[60]. The dynamics of dopamine uptake and release were quantified via continuous monitoring in human neuroblastoma cells using electrochemical sensing in a microfluidic device. The approach allowed for monitoring of the kinetics on a 1 min timescale as an indirect measure of the synaptic responses that occur on much shorter time frames (~250 ms; Table 1)[61]. Furthermore, spatial transcriptomics[62,63] and microwave technology could provide enhanced quantifications of cellular interactions and organization, cell type diversity and localization in MPSs and primary tissues (as discussed in the section 'Technical advances for the quantification of physiological features'). Also, in addition to the quantification of cell co-localization, functional readouts are necessary to confirm actual cell–cell interactions in MPSs.

Inflammatory responses. All organs contain immune cells surveilling the tissue and determining when tolerance or an immune response should occur. An inflammatory response is elicited via a complex

cascade of cellular interactions, typically to protect the body from harmful pathogens. This cascade involves the recruitment of circulatory or tissue-resident immune cells into the affected tissue and is mediated by the secretion of cytokines as a means of intercellular communication. The levels of transmigrated or infiltrated immune cells (as discussed in Supplementary Discussion 4 and Supplementary Table 1) and of cytokine secretion are thus clinically relevant proxies for the presence of inflammatory and disease states[64].

Because cytokine secretion can be quantified in serum or blood samples, it is possible to make comparisons of in vivo and in vitro cytokine concentrations within the vascular system, as was shown for a VoC system that had physiological levels of interleukin-6 (IL-6; Table 1)[65]. However, as cytokine production is local and context dependent, systemic measurements in bodily fluids should be viewed rather as useful indicators. Also, normalizations for cell number and media volume would be required to compare cytokine secretion profiles in MPSs of different dimensions (for example, in a tubular model system of the BBB, cytokine levels were normalized to endothelial cell area[66]). Moreover, because sampling of fluids from the intestine, brain and heart is often not possible, making direct in-vivo-to-in-vitro comparisons is challenging. One way to address this problem is to study relative changes in cytokine levels on exposure to reference compounds (such as model drugs) that have been studied extensively in vivo. This strategy was shown to be effective in a GoC model containing two hydrogel-separated perfusable microchannels, one of which was seeded with primary intestinal epithelial cells. Cytokines were measured in the supernatant after stimulation with lipopolysaccharide and interferon gamma to mimic the conditions of inflammatory bowel disease[67]. TPCA-1, a known anti-inflammatory compound in vivo, decreased the production of this proinflammatory cytokine by intestinal epithelial cells in a dose-dependent manner. Such inhibition was more pronounced on the basolateral space than on the apical side, underlining location-specific dynamics and the relevance of having access to both sides of polarized cell layers in MPSs. Cytokine secretion has also been measured in a 3D multicellular BoC to study neuroinflammatory responses[68]. The model consisted of hiPSC-derived neurons and astrocytes grown together with primary human microglia. The activation of microglia was confirmed via the presence of proinflammatory cytokines in the culture medium. Such a model could be useful to study relative changes induced by drugs or other reference compounds (as has been done for GoC models).

Because inflammatory responses are a feature that is often used in clinical diagnoses, the comparison of observations in MPSs and humans is valuable for disease modelling and drug discovery. As we have discussed via selected examples, data from MPSs can increasingly be compared directly with clinical outcomes. However, one should pay attention to the specifics of the quantification methods and to the scaling parameters of the model system. When direct comparisons are not possible, MPSs can be benchmarked via analyses of relative changes induced by reference compounds that are well established in vivo.

Barrier integrity. Several organs in the body embed selective barriers that aid the transport of nutrients and the protection of tissues from toxins. In particular, in the vasculature and intestine selective barriers arise from the combined effect of tight junctions and adherens junctions between endothelial cells (in the vasculature) or epithelial cells (in the intestine). Also, the intestine offers another layer of protection: the mucus covering the epithelium on the luminal side (as detailed in Supplementary Discussion 4 and Supplementary Table 1).

For both mucosal and non-mucosal tissues, the integrity of the barriers is often quantified in vitro or ex vivo by one of two methods: transendothelial/transepithelial electrical resistance (TEER) or the translocation of a fluorescent tracer. TEER is often used in MPSs, but may show inconsistency across models or even within the same model (the section 'Technical advances for the quantification of physiological features' provides considerations for the reliable quantification of barrier integrity using TEER). Tracer translocation assays are somewhat easier to use in MPSs because compartmentalization and a controlled cell area for diffusion allow good reproducibility and standardization, as has been shown in models of the BBB—probably the most intensively investigated barrier. Models of the BBB are usually based on a standard VoC system to which various types of brain cells are added (most commonly, astrocytes). Absolute values of solute permeability in vivo have been recapitulated with a range of VoC models[69]; however, some systems remain more suitable than others for direct in vivo comparison. It is important that designed features influencing barrier permeability, such as vessel geometry and flow rate, are standardized, which favours models with rectangular and tubular microchannels over those with self-assembling vascular networks, which typically show substantial variabilities in vascular diameter. For example, measurements in microchannels under continuous unidirectional flow suitable for the long-term assessment of endothelial cell permeability led to permeability values of ~70 kDa (4×10^{-7} cm s^{-1}), which is similar to the permeability of rat vessels in vivo (Table 1)[70]. Yet, the application of unidirectional flow requires more complex microfluidic setups, which generally limits the throughput of permeability measurements. This problem can be sidestepped by using microtitre plates that incorporate bidirectional flow and allow for real-time monitoring of fluorescent tracer translocation into a hydrogel lining the tissue channel[71,72], as has been shown for both VoC and GoC systems. Also, distinct fluorescent tracers can be used to quantify the bidirectional permeability of a barrier, as they are transported through passive paracellular absorption in the influx direction and through carrier-mediated transport in the efflux direction, as was shown for rhodamine 123 in a perfused GoC microchamber[73,74].

Although fluorescent tracers are valuable for comparing the permeability of different model systems with ex vivo data, comparisons with human tissues in vivo require reference compounds with known translocation properties in humans, such as certain drugs and food-derived compounds. This was exemplified in a GoC study that described the apparent permeability values of two reference molecules—caffeine and atenolol—for which the transmucosal permeability in vivo is well known[75] (Table 1). This strategy can be enhanced via the integration of electrochemical sensors that allow real-time measurement of a diverse range of compounds in the flow-through of OoCs with high sensitivity (as detailed in the section 'Technical advances for the quantification of physiological features').

Electrical signalling. Multiple tissues in the human body use electrical signals to propagate functional information from one cell to another. In the brain, electrical signals orchestrate neuronal communication, whereas in the heart they enable muscle contraction. These electrical signals are the result of a highly regulated flow of ions across the plasma membrane of individual cells. Although this basic mechanism is conserved, the tissue organization and cell morphology differ to accommodate organ-specific functions (this is discussed specifically for neuronal morphology in BoCs in Supplementary Discussion 4 and Supplementary Table 1).

The efficient conduction of membrane currents results from the specific morphology of electrically active cells. The conduction velocity of these currents within tissues depends on cell geometry and the spatial patterning of the gap junctions that connect neighbouring cells[76]. Because PDMS is transparent, voltage-sensitive dyes can be used to measure conduction velocity in tissues. A pillar-based model of heart tissue revealed that the conduction velocity in human embryonic stem cell-derived cardiomyocytes was comparable to that of a healthy human heart (Table 1)[77]. Other electrophysiological parameters (such as resting membrane potential, action potential and excitation threshold) are dependent on the abundance and localization of ion channels in the membranes of cardiomyocytes and neurons[78,79].

Measuring these features in vitro involves impaling single cells with a glass electrode (known as the whole-cell patch clamp method[80]). Similar techniques are being used to assess the electrical activity of cells in MPSs. For example, by using 3D cardiac tissue on standing pillars, impaled electrodes showed that the resting membrane potential was slightly lower than the physiological membrane potential, but that the action potential amplitude was ~97 ± 2 mV, which is close to that in mature cardiomyocytes[81] (Table 1). Measurements with sharp electrodes showed that hiPSC-derived cardiomyocytes from dissociated cardiac Biowire models had resting membrane potentials (about −97 mV) that were similar to those of adult human cardiomyocytes. However, these types of measurement are low throughput and technically challenging; thus, it would be beneficial to integrate sensors for continuous electrical readout into the devices.

Multi-electrode arrays (MEAs) are an alternative option for obtaining continuous electrophysiological measurements and are easier to use. In MPSs of the heart, MEAs have been integrated into flexible and patterned PDMS membranes, allowing for the measurement of electrical activity in aligned myocardium under the simultaneous application of mechanical strain[82]. For MPSs of the brain, 3D high-density MEAs have been used to measure cellular dynamics in 3D brain organoids[83]. These measurements revealed complex oscillatory waves that mimic neuronal activity in preterm neonates[84]. Also, highly synchronous events were detected at a burst frequency of 0.2 Hz and a local field potential of 3 Hz, which are conditions similar to those in vivo (Table 1). Newer developments include MEAs made of flexible and optically transparent electrodes (particularly electrodes made of poly(3,4-ethylenedioxythiophene):polystyrene sulfonate (PEDOT:PSS)), which allow for the imaging of cells simultaneously with the measurement of electrical field potentials[85] and the integration of flexible 3D electrodes into MEAs for the spatial mapping of tissue volumes[86]. Alternatives to these traditional electrophysiological measurements are voltage- and calcium-sensitive dyes or genetically encoded indicators of voltage and calcium, which allow for the continuous monitoring of electrical activity in cell cultures[79].

Renewal. Cell turnover and renewal rates can vary greatly. The intestine has one of the highest cell turnover rates, whereas the heart and brain have very little regenerative capacity[87]. The vasculature has a relatively slow and location-dependent turnover rate, yet retains the capacity for neovascularization and angiogenesis in wound healing.

To sustain a high turnover rate, intestinal epithelial cells undergo directional migration from the crypt to the villus tip. This process has been studied in perfused scaffold-based tubular GoC models by using 5-ethynyl-2′-deoxyurinidine (EdU) pulse–chase to monitor cell division over time[14]. Four days after the EdU pulse, all labelled cells had been shed into the luminal space and none remained in the epithelial layer, thus marking a full turnover, in line with the turnover rate of the human intestine. However, the distance that cells travel from the crypt to the villus tip in GoC models is often not representative of the distance travelled in the human intestine. An alternative approach is to quantify the migration speed of the epithelial cells; using the same EdU pulse–chase method, this was shown to be 40 µm d^{-1} in a non-perfused scaffold-guided intestinal tissue model[38]. This falls within the range measured in the small intestine of neonatal rats but is lower than the typical values measured in the intestine of mice (Table 1). A reference value for the human intestine has apparently not yet been reported.

The migration of endothelial cells during angiogenesis has been studied in VoC models using immunostaining techniques. Because angiogenesis is often associated with disease or development, extrapolating in vivo values to benchmark in vitro assays is challenging. However, VoC models provide opportunities to study which parameters might influence the angiogenic process. One such model consisted of multiple parallel microfluidic channels that can be filled with either hydrogel or culture medium to investigate how mechanical cues, such

as interstitial flow (modulated by hydrostatic pressure differences over the channels), affect angiogenesis (Table 1)[88]. Immunofluorescence imaging was used to quantify the number of angiogenic sprouts, sprout length and nuclear translocation within the sprouts at different time points. Another study quantified sprout formation kinetics using fluorescently tagged vascular and lymphatic endothelial cells in two parallel microchannels, allowing for investigation of vascular and lymph angiogenesis in the same system[89]. Incidentally, quantitative comparisons of angiogenesis in these VoC systems could benefit from consistent reporting of angiogenesis in units of µm per hour.

Technical advances for the quantification of physiological features

There are substantial limitations to the quantitative control of physiological features in MPSs. This is in part owing to a lack of awareness of the importance of reporting quantitative data that can be correlated with in vivo physiology. Also, many quantitative parameters of cell culture are impossible to engineer or measure in current MPS systems. In this section, we describe upcoming methods and technologies that could improve or enable the quantification of physiological features in one or multiple types of OoC.
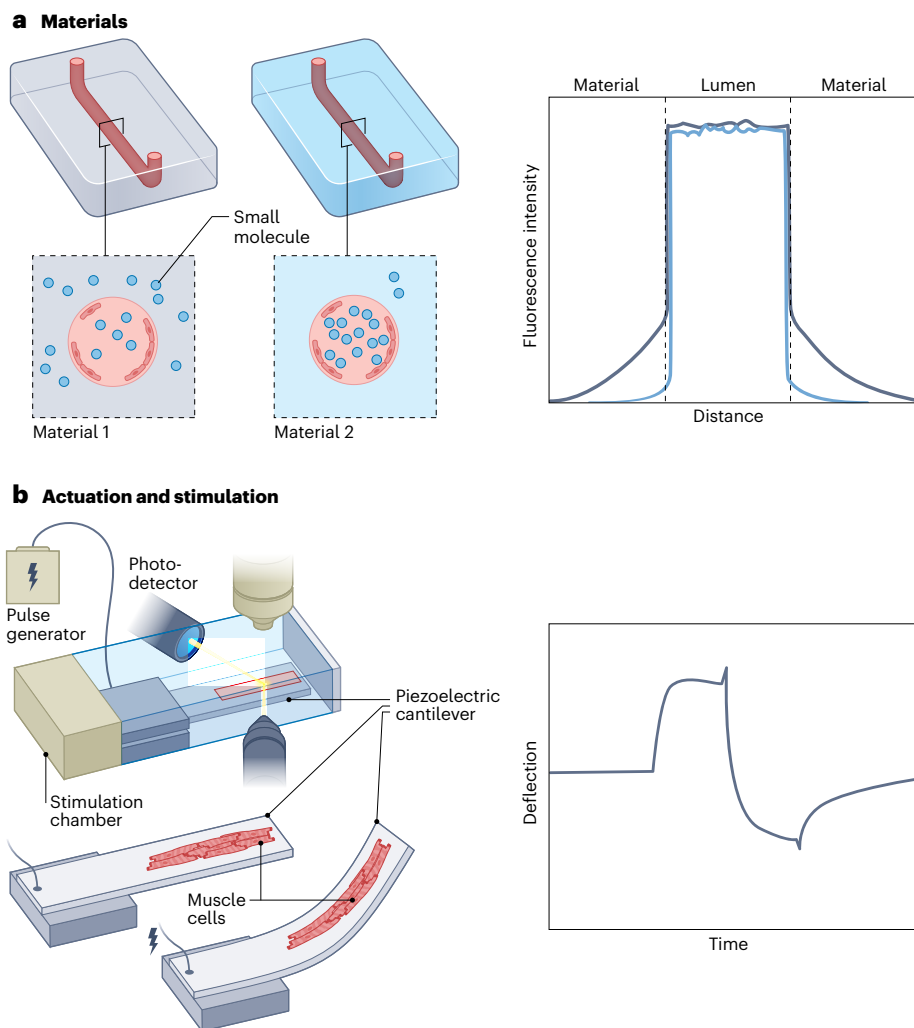
Designed features
Technical advances in device design (including its materials and any actuation and stimulation) could lead to better recapitulation of the in vivo tissue environment or architecture or improvements in the quantitative control of physiological features (Fig. 6).

Materials. The materials used in MPSs dictate biocompatibility, tissue stiffness, optical transparency, gas permeability, the absorption of small molecules and the manufacturability and reliability of the devices and can therefore profoundly impact the control of physiological features. PDMS is the most common elastomer used to manufacture MPSs; however, despite its many advantages, PDMS shows hydrophobic recovery[90], high and non-specific absorption of small hydrophobic molecules[91] and high gas permeability[92,93], which challenges the control of some physiological features. For instance, maintaining hypoxia or an oxygen gradient in VoC and GoC models requires tight regulation of the oxygen concentration. Also, PDMS may interfere with establishing growth factor gradients or measuring secreted molecules (such as neurotransmitters, cytokines or metabolized drugs). Alternatives to pristine PDMS include PDMS-based elastomers with tailored long-lasting bulk[94] and surface[95,96] hydrophilicity, TPEs and off-stoichiometric thiol-ene polymers. TPEs are biocompatible[97] and optically transparent and because they combine the properties of thermoplastics and elastomers they are amenable to high-throughput fabrication (for example, by injection moulding)[98]. Importantly, TPEs show lower small molecule absorption[99] and oxygen permeability than PDMS (2–50 versus 500 Barrer)[100]. Thiol-ene polymers are also optically transparent elastomers featuring lower small molecule absorption and more stable surface modification capabilities than PDMS and a wide range of stoichiometry-dependent stiffnesses[42]. The lower oxygen permeability of both classes of material would enable better modelling of hypoxic conditions in vessels and intestines without the need for anaerobic incubators.

Actuation and stimulation. Stimulation and actuation in MPSs are necessary to recapitulate the dynamic microenvironment in some organs. Examples of actuation are mimicking the peristaltic movement in the intestine, recreating circumferential strain in the vasculature and modelling strains in the beating heart.

Piezoelectric materials can be used for the actuation of tissues within MPSs. Unlike piezoresistive materials commonly used for strain sensing[101,102], piezoelectric materials can transduce electrical signals to mechanical movement and reciprocally sense mechanical motion to

Fig. 6 | Technical advances for the quantification of designed physiological features in MPSs. Technical advances in materials and actuation and stimulation methods may improve the recapitulation of in vivo observations and the quantitative control of designed features. **a**, Materials can be tailored for use in MPSs. In particular, new polymer formulations or targeted polymer surface functionalization could be developed to avoid the absorption of small molecules by common elastomers such as PDMS and might enhance long-term hydrophilicity to favour cell adhesion. **b**, Mechanical structures made of electrically responsive materials, such as piezoelectric materials and electroactive polymers, can enhance the local stimulation of tissues. For example, patterned piezoelectric cantilevers that bend on electrical input could provide controlled stretching to thin films of muscle or cardiac tissue. Displacement of the cantilever could be tracked by optical means and correlated to induced tissue deformation, and the inverse piezoelectric effect could in turn be exploited to detect inherent tissue motion. Panel **b** adapted with permission from ref. 103, Springer Nature Limited.

convert it to an electrical signal. They can thus be used as both micro-actuators and sensors in MPSs. Piezoelectric cantilevers have been used to electrically induce mechanical bending (and when hiPSC-derived cardiomyocytes were cultured directly on the cantilevers, their contraction dynamics and alterations on drug exposure could be sensed by the cantilevers[103]). To a lesser extent, certain types of electroactive polymers also show reciprocal transduction between mechanical and electrical signals. IPMCs are one such type of material; they offer higher biocompatibility and softness than typical piezoelectric materials[104]. Additionally, IPMCs benefit from hydration with solutions containing ions (such as phosphate-buffered saline and cell culture media), making them well suited for use in long-term cell culture experiments. Owing to their biocompatibility and low driving voltage, IPMCs can also be used as artificial muscles[105] for the mechanical stimulation of tissues[106] and as active microfluidic components such as micropumps[107,108]. Piezoelectric materials and IPMCs could conceivably be tailored to envelop tubular structures and thus induce mechanical motion; hence, they could be integrated to generate physiologically relevant circumferential strain in a vessel model, as well as peristaltic movement in an intestine model, without the need for external pressure sources and vacuum chambers. Although these materials currently exert less force than pneumatic alternatives, they hold great potential to simplify the geometry and fabrication of MPSs by enabling electrically activated movements in specified locations of the device (for instance, in membranes or pillars).

Optogenetics is an alternative method for stimulation, but it requires the genetic engineering of cells[109]. Optogenetics can be used to actuate muscle contraction accurately, and the optical transparency of MPSs would allow for local optogenetic stimulation of engineered light-sensitive tissues, as was shown with the light-driven stimulation of muscle contraction in an amyotrophic-lateral-sclerosis-on-a-chip[110].

Emergent features

There are a number of technical advances—sensing via electrical, electrochemical, optical and microwave means (Fig. 7)—that could improve the quantification or real-time monitoring of physiological features in MPSs. Most commonly used MPSs lack embedded

a Electrical sensing

b Electrochemical sensing

c Optical sensing

d Microwave sensing
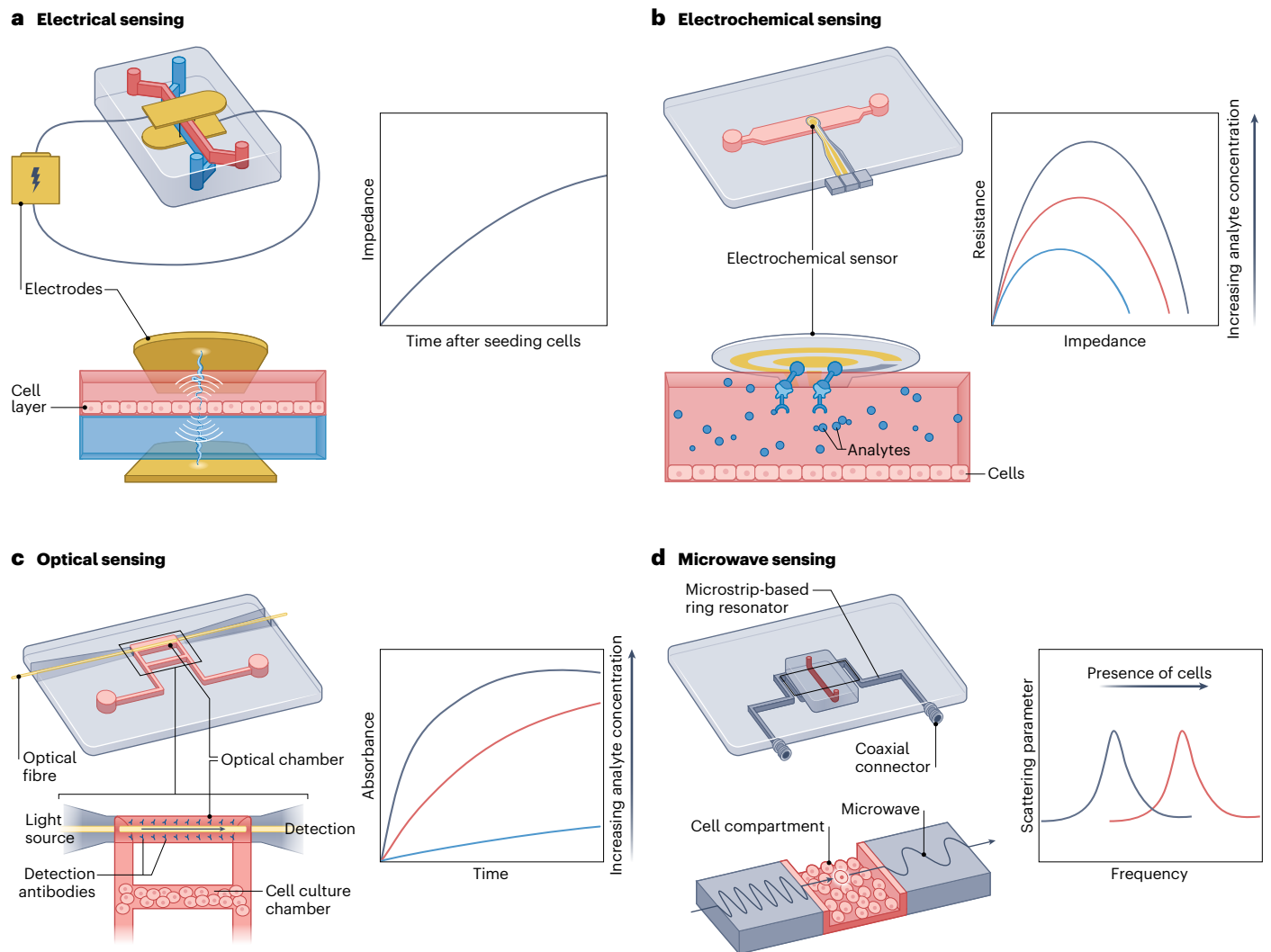
Fig. 7 | Technical advances for the quantification of emergent physiological features in MPSs. Technical advances in electrical sensing, electrochemical sensing, optical sensing and microwave sensing can yield advanced readout systems that enable or improve the quantification of emergent features. Most of these sensing solutions are based on electrodes and thin-film technology originally developed for microelectronics. Hence, the readout systems can benefit from available expertise and advantages in miniaturization, integrability and scalability. **a**, Electrical parameters of tissues, such as their resistance and capacitance (that is, electrical impedance), can be monitored continuously and correlated with their functionality (such as the tightness of a tissue barrier, or tissue composition). Measurements of transepithelial or -endothelial resistance and, more generally, impedance spectroscopy can be conducted by flanking tissues with pairs of electrodes and subjecting them to electric fields with a range of frequencies. **b**, In electrochemical sensing—amperometric or voltametric—surface chemical reactions can be exploited to trigger electrical output that correlates with changes in the local microenvironment caused by,

for example, tissue metabolism or the composition of the medium. Specific surface functionalization of the electrodes would enable higher selectivity and multiplexing. **c**, In addition to enabling optical inspection by microscopy, light waves are convenient sensing beacons because wave frequency and wave amplitude and their interference can be extremely sensitive to changes in optical path owing to medium density and transparency (as caused, for instance, by the release or selective binding of antibodies). This makes the integration of optical waveguiding structures, such as optical fibres, into MPSs appealing. **d**, Microwaves occupy a specific portion of the electromagnetic spectrum and can be injected and confined within engineered microstructures, such as ring oscillators based on microstrip lines. They are therefore useful as sensitive detectors of local changes in permittivity induced by, for example, a cellular layer or the composition of the medium. Panels adapted with permission from: **b**, ref. 130, Springer Nature Limited; **c**, ref. 134, American Chemical Society; **d**, ref. 196, Springer Nature Limited.

sensors, which limits the number of physiological features that can be quantified. Advances in the techniques that we discuss in this section can be integrated into MPSs as sensors, which would enable higher sensitivity and reliability owing to a decreased distance between the biological cue and sensor (in situ sensing). In most cases, the sensors integrated into MPSs need to be coupled to external input and/ or readout units, which may limit the portability of the MPS and its use in cell culture incubators and other conditioned environments. Ideally, portable or compact units would be embedded in the MPS under standardized interfacing (Supplementary Discussion 6).

Electrical, electrochemical, optical and microwave sensors can be used to quantify similar physiological features. Yet, because the integration of these sensing modalities within MPSs is in early development, it is premature to state which technique is best suited for the measurement of a particular feature.

Electrical sensing. TEER is probably the most widely used electrical sensing system. It is commonly employed in devices modelling barrier tissues, such as VoC, GoC and skin-on-a-chip models, for the quantitative assessment of barrier integrity. TEER typically involves direct

current at a single and low frequency (12.5 or 75 Hz in commercial systems). In contrast, impedance spectroscopy uses voltage–frequency sweeps to additionally quantify capacitive contributions to impedance in combination with equivalent electric circuit analysis[111]. Impedance spectroscopy can be useful to quantify TEER and other features, such as villus-like fold formation in GoC models[112] and the development of a multilayer epidermal structure in a skin-on-chip model[113]. However, although barrier integrity measurements are straightforward, they are prone to inconsistencies and difficult to standardize[114] (owing to a non-uniform current density over the area of cell coverage). They are also prone to monitoring a whole cell layer rather than only around the electrodes, to differences in temperature, to system-to-system geometrical and material differences, to electrode placement and measurement reproducibility and to long-term saturation of the electrodes. Nevertheless, there are correction factors for some of these parameters[115,116]. Also, sensitivity field calculations can help to optimize electrode geometry and configuration to focus the measurement on the desired device volume[117]. Higher sensitivity can be obtained via multiplexing and by specifically placing the electrodes either on the side of the culture area[118] or on membranes[119].

Sensors leveraging impedance spectroscopy can be combined with multi-electrode arrays[120] and sensors monitoring pH, oxygen content or specific biomarkers. Also, measurements of electrical impedance can be carried out via functionalization of the electrode surface with selective chemistry[121]. Impedance spectroscopy can be further improved and adapted for 3D tissues and cellular constructs[122] by integrating electrodes within confining 3D geometries (such as microfluidic traps[123] and pendant drops[124]) and in combination with 3D scaffolds[125]. Although commonly used scaffolds are made from gels or hydrogels, which are electrically passive, there are electroactive polymeric scaffolds that can be used with impedance spectroscopy. For instance, hollow tubular PEDOT:PSS structures can be used to grow intestinal epithelial cells for 26 d. The electrical properties of the PEDOT:PSS scaffold promote coupling of cells to the electrode, and by choosing the position of the electrodes carefully, both electrode mode and transistor mode sensing are possible, meaning cell substrate coverage and cell-induced volumetric constriction can be monitored in tubular structures[126].

Electrochemical sensing. Electrochemical sensors capture electrical signals arising from electrochemical interactions between analytes and electrodes. The surface of the electrodes can be functionalized with biomarkers that improve the selectivity and sensitivity of sensing[127]. Integrated within MPSs, miniature affinity-based electrochemical sensors can be used for the continuous monitoring of biomarkers, and thus provide real-time readouts of biological responses and opportunities to correct and control fluctuations within an experiment[128]. Several biochemical markers can be simultaneously sensed via multiplexing of the readouts from multiple selective electrodes[121]. Hence, electrochemical sensors can be powerful alternatives to standard protein measurements via enzyme-linked immunosorbent assays in culture medium, and enable the quantification of multiple physiological features in OoC flow-through in real time, such as secreted cytokines, biological or drug metabolites and the transport of compounds through a cell layer[129]. Functionalized electrochemical sensors have been integrated into a liver–heart OoC to measure three different biomarkers (albumin, glutathione *S*-transferase α and creatine kinase–myocardial band). The reported detection limit of albumin (0.1 ng ml^{-1}) suggests that electrochemical sensors can reach concentration ranges and sensitivities[130,131] that are superior to the common detection range of clinical tests on blood and urine (0.034–0.054 g ml^{-1} for albumin) and that quantitative comparisons of the concentration of biomarkers and small analytes in MPSs and urine or blood may be feasible.

The functionality of electrochemical sensors depends on the spatial distribution and position of the electrodes within the MPS. Hence, the integration of multiple miniaturized electrochemical sensors (particularly those leveraging field effect transistors that inherently amplify electric signals) would enhance the spatial resolution of the detection of analytes throughout the MPS[132].

Optical sensing. By measuring changes in the properties of optical waves (amplitude, wavelength and phase), optical sensors can detect changes in optical or geometrical properties (such as colour, luminescence, absorption, scattering, refractive index, size and shape). In MPSs, the changes can be caused by tissue metabolism and dynamics and by shifts in the composition of the medium (owing to changes in the concentration of an analyte of interest or an optical reporter[133]).

Optical sensors can monitor cytokines and other small biomolecules and thus provide opportunities for the standardization of MPSs. For example, the integration of an optical fibre-based sensing unit with a microfluidic setup was used to quantify IL-2 secreted by lymphocytes[134] (IL-2 concentrations in the range of 50–1,000 pg ml^{-1} could be measured within 30 min). A multiplexed version of this system leveraging an array of silicon photonic micro-ring resonators may allow for the simultaneous and continuous quantification of multiple cytokines. Specifically, the shifts in resonance wavelength on binding of the target molecule to the ring surface would enable discrimination of the different cytokines without the need for specific labelling (which current techniques require[135]).

The quantification of tissue architecture, cell morphology, mucus layer thickness, cell surface area, fluid flow rates and many other physiological features in MPSs often relies on imaging technologies that can penetrate tissues and substrate materials while maintaining good resolution. In particular, optical coherence tomography allows for real-time imaging of relatively large structures in MPSs without the need for immunostaining or fluorescent reporters[136]. The technique relies on measurements of the interference between a reference light beam and backscattered light for reconstruction of the profile of the sample. Although the depth of imaging of optical coherence tomography can reach >1 mm (ref. 137), the technique's typical spatial resolution (~6 μm) is somewhat lower than that of conventional microscopy (<1 μm)[138]. Nevertheless, it enables the continuous monitoring and quantification of 3D structures in MPSs, as was shown for sprouting angiogenesis in a VoC model[138] and engineered microvessels in an MPS of the outer blood–retinal barrier[139].

Microwave sensing. Similar to electrical impedance and optical sensing, electromagnetic waves in the microwave range (~1–40 GHz) can also be used for contactless sensing. In this case, the sensing principle is based on measuring how the electromagnetic waves interact with materials. The degree of penetration of the waves into a material depends on the frequency and electrical characteristics of the material (mainly its permittivity). Electromagnetic waves at microwave frequencies can penetrate cells, leaving them intact[140], and reveal information about intracellular composition[141]. Hence, microwave sensing allows for the label-free and non-intrusive real-time discrimination, localization and counting of cells[142] and can be particularly useful for the quantification of cell type ratios in MPSs.

A microwave sensor based on impedance spectroscopy allowed for the label-free identification of cell diversity at the single-cell level at microwave frequencies[140], and a flow-through sensor within an integrated multimode microwave resonator was used to distinguish two different cancer cell lines in mixed cell populations[143]. Further integration of real-time microwave sensors may improve the quantification of different cell types within a culture system and reveal spatial information of individual cells within 3D tissue. Real-time information about the numbers and ratios of different cell types in MPSs will facilitate the standardized quantification of physiological features that need to be normalized to specific cell type numbers.

Additionally, microwave-supporting structures such as resonators and microstrip lines can be embedded into microfluidic systems as part of highly sensitive sensors with an electrical readout for flow rates and fluid composition. For example, split-ring microwave resonators coupled to an interferometric system allowed for high-sensitivity measurements of glucose concentration in a microfluidic setup[144]. Also, a fluid flow sensor embedded in a microfluidic device exploited the flow rate-dependent deformation of a thin circular membrane integrated within a planar microwave ring resonator, as well subsequent alteration of the effective permittivity of the surrounding medium, to measure flow rates in the range of 0.5–300 µl min^{-1} with a resolution of 1 µl min^{-1} (ref. 145). These and similar systems need to be supported by accurate analytical and numerical models for the prediction of sensor performance[146] and by electronic readout systems that can be integrated into compact layers (such as printed circuit boards) connected to the sensors.

Outlook

MPSs are poised to substantially contribute to biomedical research. Yet, to advance the technology towards greater end user and regulatory acceptance, it is essential to understand its predictive value. With the growing number of users, it is widely accepted that consensus on qualification and standardization methods for MPSs is urgent. Quantification of physiological features in MPSs may lead the way towards establishing accurate comparisons between different in vitro models and in vivo physiology, contributing to the development of measurable standards to qualify MPSs as fit for purpose in applications. We hope that the overview of quantifiable physiological features of healthy organ function in MPSs that we provide in this Perspective serves as a resource for the development of such measurable standards, and that these standards can be used as a basis for the quantification of disease phenotypes and of drug efficacy and toxicity (which can be defined as deviations in the same physiological features). These types of quantification will be central to establishing the predictive value of MPSs and accelerating their implementation in the drug development pipeline.

MPSs are particularly suitable for providing quantitative approximations of physiological features, as the devices allow for versatile design and the integration of sensors and readout methods. Categorizing the desired quantifiable physiological features as designed features (that can be controlled in MPS design) and emergent features (that describe cellular function) will facilitate quantification in MPSs, as both types of feature require different strategies. For quantifying designed features, it is essential to consider the relevant technology and materials needed to incorporate a specific feature in the desired range. Quantification of emergent features requires the incorporation of relevant sensing and readout systems to accurately monitor cellular responses using standardized methods and units. To further steer the exact value of an emergent feature, which might be required to qualify the system as fit for purpose, the designed features that influence the emergent feature need to be determined and adapted. The examples and considerations highlighted in this Perspective will help users to select the relevant design options and sensing technologies to optimize the quantification of the designed and emergent features of interest.

Although MPSs generally aim to mimic the in vivo architecture of a tissue, the main goal is to recapitulate one or multiple functional features of the tissue or organ. As such, they do not necessarily have to recapitulate the dimensions of the human body. When functional features are influenced by the dimensions of the tissue, scaling and normalization become a necessity. To compare in vitro MPSs with in vivo measurements, it is essential to correct for differences in surface-to-volume and cell-to-volume ratios[147]. In some cases, it might be sufficient to simply normalize to the liquid volume, number of cells and dimensions (in particular when converting the absolute fluid flow rate to wall shear stress). For more complex features and

systems, in silico modelling may be necessary (as was shown for multi-organ systems[148]).

Quantitative comparisons of physiological features in MPSs with in vivo observations are limited, mostly by differences in scale, methods of quantification and resolution and duration. When the quantification method of a specific physiological feature differs between systems, it becomes more difficult to compare data accurately. For instance, for emergent features that describe complex cellular functions, many different quantification methods and units are used. More clarity is needed on how data are measured and reported in clinical settings and on whether it is feasible to replicate these data in model systems. For certain features, such as the measurement of secreted products in circulation and flow-through, it can be straightforward; for others, such as the measurement of barrier integrity, it can be difficult. For physiological features that are not amenable to using a single translatable measurement method, consensus should be reached on how to quantify and report the data in a standardized manner. For a few notable physiological features, in this Perspective we have outlined a basis for the standardization of quantification methods and data reporting. Some of these features, such as cytokine secretion, are location and time dependent and can be quantified at high resolution in MPSs but not in vivo. One solution is to focus on the relative changes in cellular function induced by clinically tested reference compounds. These will be valuable benchmark measures for drug development and should facilitate the uptake of MPSs by regulatory authorities and pharmaceutical companies. Coupling multi-organ chips may eventually allow for the modelling of local and systemic responses.

At present, MPSs are designed to recapitulate and facilitate the monitoring of aspects of tissue physiology and pathophysiology over relatively short periods of days or weeks. Likewise, in MPSs the responses of the tissues to drugs and their clearance are acute. Chronic responses cannot typically be monitored; in fact, there are only a few examples of long-term cell culture in these devices. Advances in materials, pumps and sensors, as well as culture media that better mimic body fluids, will be needed to model chronic phenomena and to couple multiple MPSs in series or parallel to recapitulate the organ–organ and tissue–tissue interactions in the human body.

Advancing MPSs will require greater precision in detecting what MPSs actually capture. Are the tissue responses typical of tissues and organs that are foetal, adult or aged? Are pathological responses correctable by therapeutic interventions, and are their timings relevant compared with the actual progression of the disease? The quantitative approach outlined in this Perspective should help to address these questions.

We regard the concept of quantitatively measuring designed and emergent physiological features as an important first step towards a publicly available database that facilitates the benchmarking of a diverse range of MPSs to other MPSs and in vivo data. One strategy would be to create a freely available MPS atlas akin to the Human Cell Atlas (https://www.humancellatlas.org). The adapted mission statement could be similar: to create comprehensive references of all human MPSs as a basis for understanding human health and for diagnosing, monitoring and treating disease. Such an atlas could contain available quantifications of designed and emergent physiological features for a wide range of MPSs and function as a reference dataset that provides insight into which designed features are important to implement in an MPS in order to obtain a desired emergent feature.

In summary, the considerations described in this Perspective are relevant for improving the quantification, standardization and extrapolation of data from in vitro conditions to in vivo settings. Notably, with the many technical options available for designing MPSs and integrating sensors and readouts, it becomes increasingly important to report the rationale of certain design choices and how they relate to the physiology that is recapitulated. Moreover, reporting the quantitative output of MPSs in a comparable and translatable way will highlight

the potency of these models for accurately predicting and replicating specific physiological processes. More emphasis and discussion on the quantification of physiological features in MPSs, rather than their qualitative implementation, will be essential to define measurable standards for model standardization in a time of rapidly increasing numbers of MPS designs and users.

References

1. Ingber, D. E. Human organs-on-chips for disease modelling, drug development and personalized medicine. *Nat. Rev. Genet.* **23**, 467–491 (2022).
2. Vunjak-Novakovic, G., Ronaldson-Bouchard, K. & Radisic, M. Organs-on-a-chip models for biological research. *Cell* **184**, 4597–4611 (2021).
3. Mastrangeli, M., Millet, S. & van den Eijnden-Van Raaij, J. Organ-on-chip in development: towards a roadmap for organs-on-chip. *ALTEX* **36**, 650–668 (2019).
4. Ingber, D. E. Reverse engineering human pathophysiology with organs-on-chips. *Cell* **164**, 1105–1109 (2016).
5. Low, L. A., Mummery, C. L., Berridge, B. R., Austin, C. P. & Tagle, D. A. Organs-on-chips: into the next decade. *Nat. Rev. Drug Discov.* **20**, 345–361 (2020).
6. Mastrangeli, M. et al. Building blocks for a European organ-on-chip roadmap. *ALTEX* **36**, 481–492 (2019).
7. Wu, Z. et al. Microfluidic printing of tunable hollow microfibers for vascular tissue engineering. *Adv. Mater. Technol.* **6**, 2000683 (2021).
8. Linville, R. M. et al. Human iPSC-derived blood–brain barrier microvessels: validation of barrier function and endothelial cell behavior. *Biomaterials* **190–191**, 24–37 (2019).
9. De Graaf, M. N. S. et al. Scalable microphysiological system to model three-dimensional blood vessels. *APL Bioeng.* **3**, 026105 (2019).
10. Kim, S., Lee, H., Chung, M. & Jeon, N. L. Engineering of functional, perfusable 3D microvascular networks on a chip. *Lab Chip* **13**, 1489–1500 (2013).
11. Campisi, M. et al. 3D self-organized microvascular model of the human blood–brain barrier with endothelial cells, pericytes and astrocytes. *Biomaterials* **180**, 117–129 (2018).
12. Brandenberg, N. & Lutolf, M. P. In situ patterning of microfluidic networks in 3D cell-laden hydrogels. *Adv. Mater.* **28**, 7450–7456 (2016).
13. Enrico, A. et al. Three dimensional microvascularized tissue models by laser-based cavitation molding of collagen. *Adv. Mater.* **34**, 2109823 (2022).
14. Nikolaev, M. et al. Homeostatic mini-intestines through scaffold-guided organoid morphogenesis. *Nature* **585**, 574–578 (2020).
15. MacQueen, L. A. et al. A tissue-engineered scale model of the heart ventricle. *Nat. Biomed. Eng.* **2**, 930–941 (2018).
16. Chen, Y. et al. A microfluidic circulatory system integrated with capillary-assisted pressure sensors. *Lab Chip* **17**, 653–662 (2017).
17. Sarkar, A. et al. Efficient generation of CA3 neurons from human pluripotent stem cells enables modeling of hippocampal connectivity in vitro. *Cell Stem Cell* **22**, 684–697 (2018).
18. Dauth, S. et al. Neurons derived from different brain regions are inherently different in vitro: a novel multiregional brain-on-a-chip. *J. Neurophysiol.* **117**, 1320–1341 (2017).
19. Odawara, A., Gotoh, M. & Suzuki, I. A three-dimensional neuronal culture technique that controls the direction of neurite elongation and the position of soma to mimic the layered structure of the brain. *RSC Adv.* **3**, 23620–23630 (2013).
20. Song, J. W. et al. Computer-controlled microcirculatory support system for endothelial cell culture and shearing. *Anal. Chem.* **77**, 3993–3999 (2005).
21. Arora, S., Lam, A. J. Y., Cheung, C., Yim, E. K. F. & Toh, Y. C. Determination of critical shear stress for maturation of human pluripotent stem cell-derived endothelial cells towards an arterial subtype. *Biotechnol. Bioeng.* **116**, 1164–1175 (2019).
22. Chen, H. et al. Cardiac-like flow generator for long-term imaging of endothelial cell responses to circulatory pulsatile flow at microscale. *Lab Chip* **13**, 2999–3007 (2013).
23. Satoh, T. et al. A pneumatic pressure-driven multi-throughput microfluidic circulation culture system. *Lab Chip* **16**, 2339–2348 (2016).
24. Kim, H., Huh, D., Hamilton, G. & Ingber, D. Human gut-on-a-chip inhabited by microbial flora that experiences intestinal peristalsis-like motions and flow. *Lab Chip* **12**, 2165–2174 (2012).
25. Wasson, E. M., Dubbin, K. & Moya, M. L. Go with the flow: modeling unique biological flows in engineered in vitro platforms. *Lab Chip* **21**, 2095–2120 (2021).
26. Shin, Y. C. et al. Three-dimensional regeneration of patient-derived intestinal organoid epithelium in a physiodynamic mucosal interface-on-a-chip. *Micromachines* **11**, 663 (2020).
27. Dessalles, C. A., Ramón-Lozano, C., Babataheri, A. & Barakat, A. I. Luminal flow actuation generates coupled shear and strain in a microvessel-on-chip. *Biofabrication* **14**, 015003 (2021).
28. Parsa, H., Wang, B. Z. & Vunjak-Novakovic, G. A microfluidic platform for the high-throughput study of pathological cardiac hypertrophy. *Lab Chip* **17**, 3264–3271 (2017).
29. Rodriguez, M. L., Werner, T. R., Becker, B., Eschenhagen, T. & Hirt, M. N. Magnetics-based approach for fine-tuning afterload in engineered heart tissues. *ACS Biomater. Sci. Eng.* **5**, 3663–3675 (2019).
30. Gordon, E., Schimmel, L. & Frye, M. The importance of mechanical forces for in vitro endothelial cell biology. *Front. Physiol.* **11**, 684 (2020).
31. Schroer, A., Pardon, G., Castillo, E., Blair, C. & Pruitt, B. Engineering hiPSC cardiomyocyte in vitro model systems for functional and structural assessment. *Prog. Biophys. Mol. Biol.* **144**, 3–15 (2019).
32. Onfroy-Roy, L., Hamel, D., Foncy, J., Malaquin, L. & Ferrand, A. Extracellular matrix mechanical properties and regulation of the intestinal stem cells: when mechanics control fate. *Cells* **9**, 2629 (2020).
33. Barnes, J. M., Przybyla, L. & Weaver, V. M. Tissue mechanics regulate brain development, homeostasis and disease. *J. Cell Sci.* **130**, 71–82 (2017).
34. Mason, B. N., Starchenko, A., Williams, R. M., Bonassar, L. J. & Reinhart-King, C. A. Tuning three-dimensional collagen matrix stiffness independently of collagen concentration modulates endothelial cell behavior. *Acta Biomater.* **9**, 4635–4644 (2013).
35. Soofi, S. S., Last, J. A., Lliensiek, S. J., Nealey, P. F. & Murphy, C. J. Elastic modulus of Matrigel as determined by AFM. *J. Struct. Biol.* **167**, 216–219 (2009).
36. Fuard, D., Tzvetkova-Chevolleau, T., Decossas, S., Tracqui, P. & Schiavone, P. Optimization of poly-di-methyl-siloxane (PDMS) substrates for studying cellular adhesion and motility. *Microelectron. Eng.* **85**, 1289–1293 (2008).
37. Cho, A. N. et al. Microfluidic device with brain extracellular matrix promotes structural and functional maturation of human brain organoids. *Nat. Commun.* **12**, 4730 (2021).
38. Wang, Y. et al. A microengineered collagen scaffold for generating a polarized crypt–villus architecture of human small intestinal epithelium. *Biomaterials* **128**, 44–55 (2017).
39. Pasqualini, F. S. et al. Traction force microscopy of engineered cardiac tissues. *PLoS ONE* **13**, e0194706 (2018).
40. Trappmann, B. et al. Matrix degradability controls multicellularity of 3D cell migration. *Nat. Commun.* **8**, 371 (2017).

41. Roy, E., Galas, J.-C. & Veres, T. Thermoplastic elastomers for microfluidics: towards a high-throughput fabrication method of multilayered microfluidic devices. *Lab Chip* **11**, 3193 (2011).

42. Carlborg, C. F., Haraldsson, T., Öberg, K., Malkoch, M. & van der Wijngaart, W. Beyond PDMS: off-stoichiometry thiol–ene (OSTE) based soft lithography for rapid prototyping of microfluidic devices. *Lab Chip* **11**, 3136 (2011).

43. Radisic, M. & Loskill, P. Beyond PDMS and membranes: new materials for organ-on-a-chip devices. *ACS Biomater. Sci. Eng.* **7**, 2861–2863 (2021).

44. Buguin, A., Li, M. H., Silberzan, P., Ladoux, B. & Keller, P. Micro-actuators: when artificial muscles made of nematic liquid crystal elastomers meet soft lithography. *J. Am. Chem. Soc.* **128**, 1088–1089 (2006).

45. Guin, T. et al. Layered liquid crystal elastomer actuators. *Nat. Commun.* **9**, 2531 (2018).

46. Park, T. E. et al. Hypoxia-enhanced Blood-Brain Barrier Chip recapitulates human barrier function and shuttling of drugs and antibodies. *Nat. Commun.* **10**, 2621 (2019).

47. Veldhuizen, J. et al. Cardiac ischemia on-a-chip to investigate cellular and molecular response of myocardial tissue under hypoxia. *Biomaterials* **281**, 121336 (2022).

48. Jalili-firoozinezhad, S. et al. A complex human gut microbiome cultured in an anaerobic intestine-on-a-chip. *Nat. Biomed. Eng.* **3**, 520–531 (2019).

49. Lam, S. F., Shirure, V. S., Chu, Y. E., Soetikno, A. G. & George, S. C. Microfluidic device to attain high spatial and temporal control of oxygen. *PLoS ONE* **13**, e0209574 (2018).

50. Moerkens, R. et al. An iPSC-derived small intestine-on-chip with self-organizing epithelial, mesenchymal, and neural cells. *Cell Rep.* **43**, 114247 (2024).

51. Rifes, P. et al. Modeling neural tube development by differentiation of human embryonic stem cells in a microfluidic WNT gradient. *Nat. Biotechnol.* **38**, 1265–1273 (2020).

52. Chen, L. J. et al. Single-cell RNA sequencing unveils unique transcriptomic signatures of endothelial cells and role of ENO1 in response to disturbed flow. *Proc. Natl Acad. Sci. USA* **121**, e2318904121 (2024).

53. Lee, S. et al. Angiogenesis-on-a-chip coupled with single-cell RNA sequencing reveals spatially differential activations of autophagy along angiogenic sprouts. *Nat. Commun.* **15**, 230 (2024).

54. Chen, M. B., Srigunapalan, S., Wheeler, A. R. & Simmons, C. A. A 3D microfluidic platform incorporating methacrylated gelatin hydrogels to study physiological cardiovascular cell–cell interactions. *Lab Chip* **13**, 2591–2598 (2013).

55. Hinman, S. S., Wang, Y. & Allbritton, N. L. Photopatterned membranes and chemical gradients enable scalable phenotypic organization of primary human colon epithelial models. *Anal. Chem.* **91**, 15240–15247 (2019).

56. Elmentaite, R. et al. Single-cell sequencing of developing human gut reveals transcriptional links to childhood Crohn's disease. *Dev. Cell* **55**, 771–783 (2020).

57. Xue, X. et al. A patterned human neural tube model using microfluidic gradients. *Nature* **628**, 391–399 (2024).

58. Winkelman, M. A. et al. Interstitial flow enhances the formation, connectivity, and function of 3D brain microvascular networks generated within a microfluidic device. *Lab Chip* **22**, 170–192 (2022).

59. Iannielli, A. et al. Reconstitution of the human nigro-striatal pathway on-a-chip reveals OPA1-dependent mitochondrial defects and loss of dopaminergic synapses. *Cell Rep.* **29**, 4646–4656 (2019).

60. Yu, Y. et al. A microfluidic platform for continuous monitoring of dopamine homeostasis in dopaminergic cells. *Microsyst. Nanoeng.* **5**, 10 (2019).

61. Ford, C. P., Phillips, P. E. M. & Williams, J. T. The time course of dopamine transmission in the ventral tegmental area. *J. Neurosci.* **29**, 13344–13352 (2009).

62. Vickovic, S. et al. High-definition spatial transcriptomics for in situ tissue profiling. *Nat. Methods* **16**, 987–990 (2019).

63. Srivatsan, S. R. et al. Embryo-scale, single-cell spatial transcriptomics. *Science* **373**, 111–117 (2021).

64. Fajgenbaum, D. C. & June, C. H. Cytokine storm. *N. Engl. J. Med.* **383**, 2255–2273 (2020).

65. Hajal, C. et al. Engineered human blood–brain barrier microfluidic model for vascular permeability analyses. *Nat. Protoc.* **17**, 95–128 (2022).

66. Herland, A. et al. Distinct contributions of astrocytes and pericytes to neuroinflammation identified in a 3D human blood–brain barrier on a chip. *PLoS ONE* **11**, e0150360 (2016).

67. Beaurivage, C. et al. Development of a human primary gut-on-a-chip to model inflammatory processes. *Sci. Rep.* **10**, 21475 (2020).

68. Park, J. et al. A 3D human triculture system modeling neurodegeneration and neuroinflammation in Alzheimer's disease. *Nat. Neurosci.* **21**, 941–951 (2018).

69. Hajal, C., Roi, B., Le, Kamm, R. D. & Maoz, B. M. Biology and models of the blood–brain barrier. *Annu. Rev. Biomed. Eng.* **23**, 359–384 (2021).

70. Qiu, Y. et al. Microvasculature-on-a-chip for the long-term study of endothelial barrier dysfunction and microvascular obstruction in disease. *Nat. Biomed. Eng.* **2**, 453–463 (2018).

71. Naumovska, E. et al. Direct on-chip differentiation of intestinal tubules from induced pluripotent stem cells. *Int. J. Mol. Sci.* **21**, 4964 (2020).

72. Van Duinen, V. et al. 96 perfusable blood vessels to study vascular permeability in vitro. *Sci. Rep.* **7**, 18071 (2017).

73. Tan, H. Y. et al. A multi-chamber microfluidic intestinal barrier model using Caco-2 cells for drug transport studies. *PLoS ONE* **13**, e0197101 (2018).

74. Shim, K. Y. et al. Microfluidic gut-on-a-chip with three-dimensional villi structure. *Biomed. Microdevices* **19**, 37 (2017).

75. Pocock, K. et al. Intestine-on-a-chip microfluidic model for efficient in vitro screening of oral chemotherapeutic uptake. *ACS Biomater. Sci. Eng.* **3**, 951–959 (2017).

76. Yang, X., Pabon, L. & Murry, C. E. Engineering adolescence: maturation of human pluripotent stem cell-derived cardiomyocytes. *Circ. Res.* **114**, 511–523 (2014).

77. Thavandiran, N. et al. Design and formulation of functional pluripotent stem cell-derived cardiac microtissues. *Proc. Natl Acad. Sci. USA* **110**, E4698–E4707 (2013).

78. Zwi, L. et al. Cardiomyocyte differentiation of human induced pluripotent stem cells. *Circulation* **120**, 1513–1523 (2009).

79. Van Meer, B. J., Tertoolen, L. G. J. & Mummery, C. L. Measuring physiological responses of human pluripotent stem cell derived cardiomyocytes to drugs and disease. *Stem Cells* **34**, 2008–2015 (2016).

80. Brandao, K. O., Tabel, V. A., Atsma, D. E., Mummery, C. L. & Davis, R. P. Human pluripotent stem cell models of cardiac disease: from mechanisms to therapies. *Dis. Model. Mech.* **10**, 1039–1059 (2017).

81. Tiburcy, M. et al. Defined engineered human myocardium with advanced maturation for applications in heart failure modeling and repair. *Circulation* **135**, 1832–1847 (2017).

82. Gaio, N. et al. Cytostretch, an organ-on-chip platform. *Micromachines* **7**, 120 (2016).

83. Shin, H. et al. 3D high-density microelectrode array with optical stimulation and drug delivery for investigating neural circuit dynamics. *Nat. Commun.* **12**, 492 (2021).

84. Trujillo, C. A. et al. Complex oscillatory waves emerging from cortical organoids model early human brain network development. *Cell Stem Cell* **25**, 558–569 (2019).

85. Blau, A. et al. Flexible, all-polymer microelectrode arrays for the capture of cardiac and neuronal signals. *Biomaterials* **32**, 1778–1786 (2011).

86. Soscia, D. A. et al. A flexible 3-dimensional microelectrode array for in vitro brain models. *Lab Chip* **20**, 901–911 (2020).

87. Sender, R. & Milo, R. The distribution of cellular turnover in the human body. *Nat. Med.* **27**, 45–48 (2021).

88. Kim, S., Chung, M. & Jeon, N. L. Three-dimensional biomimetic model to reconstitute sprouting lymphangiogenesis in vitro. *Biomaterials* **78**, 115–128 (2016).

89. Osaki, T., Serrano, J. C. & Kamm, R. D. Cooperative effects of vascular angiogenesis and lymphangiogenesis. *Regen. Eng. Transl. Med.* **4**, 120–132 (2018).

90. Eddington, D. T., Puccinelli, J. P. & Beebe, D. J. Thermal aging and reduced hydrophobic recovery of polydimethylsiloxane. *Sens. Actuators B Chem.* **114**, 170–172 (2006).

91. Van Meer, B. J. et al. Small molecule absorption by PDMS in the context of drug response bioassays. *Biochem. Biophys. Res. Commun.* **482**, 323–328 (2017).

92. Lamberti, A., Marasso, S. L. & Cocuzza, M. PDMS membranes with tunable gas permeability for microfluidic applications. *RSC Adv.* **4**, 61415–61419 (2014).

93. Firpo, G., Angeli, E., Repetto, L. & Valbusa, U. Permeability thickness dependence of polydimethylsiloxane (PDMS) membranes. *J. Memb. Sci.* **481**, 1–8 (2015).

94. O'Brien, D. J. et al. Systematic characterization of hydrophilized polydimethylsiloxane. *J. Microelectromech. Syst.* **29**, 1216–1224 (2020).

95. Nakano, H., Kakinoki, S. & Iwasaki, Y. Long-lasting hydrophilic surface generated on poly(dimethyl siloxane) with photoreactive zwitterionic polymers. *Colloids Surf. B Biointerfaces* **205**, 111900 (2021).

96. Holczer, E. & Fürjes, P. Effects of embedded surfactants on the surface properties of PDMS; applicability for autonomous microfluidic systems. *Microfluid. Nanofluidics* **21**, 81 (2017).

97. Schneider, S., Brás, E. J. S., Schneider, O., Schlünder, K. & Loskill, P. Facile patterning of thermoplastic elastomers and robust bonding to glass and thermoplastics for microfluidic cell culture and organ-on-chip. *Micromachines* **12**, 575 (2021).

98. McMillan, A. H. et al. Rapid fabrication of membrane-integrated thermoplastic elastomer microfluidic devices. *Micromachines* **11**, 731 (2020).

99. Lachaux, J. et al. Thermoplastic elastomer with advanced hydrophilization and bonding performances for rapid (30 s) and easy molding of microfluidic devices. *Lab Chip* **17**, 2581–2594 (2017).

100. Busek, M. et al. Thermoplastic elastomer (TPE)–poly(methyl methacrylate) (PMMA) hybrid devices for active pumping PDMS-free organ-on-a-chip systems. *Biosensors* **11**, 162 (2021).

101. Kim, D. S., Jeong, Y. J., Lee, B. K., Shanmugasundaram, A. & Lee, D. W. Piezoresistive sensor-integrated PDMS cantilever: a new class of device for measuring the drug-induced changes in the mechanical activity of cardiomyocytes. *Sens. Actuators B Chem.* **240**, 566–572 (2017).

102. Lind, J. U. et al. Instrumented cardiac microphysiological devices via multimaterial three-dimensional printing. *Nat. Mater.* **16**, 303–308 (2017).

103. Coln, E. A. et al. Piezoelectric bioMEMS cantilever for measurement of muscle contraction and for actuation of mechanosensitive cells. *MRS Commun.* **9**, 1186–1192 (2019).

104. Wang, Y. & Sugino, T. in *Actuators* 39–56 (InTech, 2018).

105. He, Q. et al. Review on improvement, modeling, and application of ionic polymer metal composite artificial muscle. *J. Bionic Eng.* **19**, 279–298 (2022).

106. Mastrangeli, M. et al. Microelectromechanical Organs-on-Chip. *Proc. 21st International Conference on Solid-State Sensors, Actuators and Microsystems (Transducers)* 102–107 (IEEE, 2021).

107. Mirfakhrai, T., Madden, J. D. W. & Baughman, R. H. Polymer artificial muscles. *Mater. Today* **10**, 30–38 (2007).

108. Annabestani, M. & Fardmanesh, M. Ionic electro active polymer-based soft actuators and their applications in microfluidic micropumps, microvalves, and micromixers: a review. Preprint at https://doi.org/10.48550/arXiv.1904.07149 (2019).

109. Emiliani, V. et al. Optogenetics for light control of biological systems. *Nat. Rev. Methods Primers* **2**, 55 (2022).

110. Osaki, T., Uzel, S. G. M. & Kamm, R. D. Microphysiological 3D model of amyotrophic lateral sclerosis (ALS) from human iPS-derived muscle cells and optogenetic motor neurons. *Sci. Adv.* **4**, eaat5847 (2018).

111. Gerasimenko, T. et al. Impedance spectroscopy as a tool for monitoring performance in 3D models of epithelial tissues. *Front. Bioeng. Biotechnol.* **7**, 474 (2020).

112. Van der Helm, M. W. et al. Non-invasive sensing of transepithelial barrier function and tissue differentiation in organs-on-chips using impedance spectroscopy. *Lab Chip* **19**, 452–463 (2019).

113. Groeber, F. et al. Impedance spectroscopy for the non-destructive evaluation of in vitro epidermal models. *Pharm. Res.* **32**, 1845–1854 (2015).

114. Holzreuter, M. A. & Segerink, L. I. Innovative electrode and chip designs for transendothelial electrical resistance measurements in organs-on-chips. *Lab Chip* **24**, 1121–1134 (2024).

115. Yeste, J. et al. Geometric correction factor for transepithelial electrical resistance measurements in transwell and microfluidic cell cultures. *J. Phys. D Appl. Phys.* **49**, 375401 (2016).

116. Blume, L. F., Denker, M., Gieseler, F. & Kunze, T. Temperature corrected transepithelial electrical resistance (TEER) measurement to quantify rapid changes in paracellular permeability. *Pharmazie* **65**, 19–24 (2010).

117. Grimnes, S. & Martinsen, Ø. G. Sources of error in tetrapolar impedance measurements on biomaterials and other ionic conductors. *J. Phys. D Appl. Phys.* **40**, 9 (2007).

118. Bossink, E. G. B. M., Zakharova, M., De Bruijn, D. S., Odijk, M. & Segerink, L. I. Measuring barrier function in organ-on-chips with cleanroom-free integration of multiplexable electrodes. *Lab Chip* **21**, 2040–2049 (2021).

119. Matthiesen, I., Voulgaris, D., Nikolakopoulou, P., Winkler, T. E. & Herland, A. Continuous monitoring reveals protective effects of *N*-acetylcysteine amide on an isogenic microphysiological model of the neurovascular unit. *Small* **17**, e2101785 (2021).

120. Maoz, B. M. et al. Organs-on-chips with combined multi-electrode array and transepithelial electrical resistance measurement capabilities. *Lab Chip* **17**, 2294–2302 (2017).

121. Liu, F., Ni, L. & Zhe, J. Lab-on-a-chip electrical multiplexing techniques for cellular and molecular biomarker detection. *Biomicrofluidics* **12**, 021501 (2018).

122. De León, S. E., Pupovac, A. & McArthur, S. L. Three-dimensional (3D) cell culture monitoring: opportunities and challenges for impedance spectroscopy. *Biotechnol. Bioeng.* **117**, 1230–1240 (2020).

123. Curto, V. F., Ferro, M. P., Mariani, F., Scavetta, E. & Owens, R. M. A planar impedance sensor for 3D spheroids. *Lab Chip* **18**, 933–943 (2018).

124. Schmid, Y. R. F., Bürgel, S. C., Misun, P. M., Hierlemann, A. & Frey, O. Electrical impedance spectroscopy for microtissue spheroid analysis in hanging-drop networks. *ACS Sens.* **1**, 1028–1035 (2016).

125. Alexander, F., Eggert, S. & Price, D. Label-free monitoring of 3D tissue models via electrical impedance spectroscopy. *Bioanal. Rev.* **2**, 111–134 (2019).

126. Moysidou, C. M. et al. 3D bioelectronic model of the human intestine. *Adv. Biol.* **5**, 2000306 (2021).

127. Zhu, Y. et al. State of the art in integrated biosensors for organ-on-a-chip applications. *Curr. Opin. Biomed. Eng.* **19**, 100309 (2021).

128. Kieninger, J., Weltin, A., Flamm, H. & Urban, G. A. Microsensor systems for cell metabolism—from 2D culture to organ-on-chip. *Lab Chip* **18**, 1274–1291 (2018).

129. Oliveira, M., Conceição, P., Kant, K., Ainla, A. & Diéguez, L. Electrochemical sensing in 3D cell culture models: new tools for developing better cancer diagnostics and treatments. *Cancers (Basel)* **13**, 1381 (2021).

130. Aleman, J., Kilic, T., Mille, L. S., Shin, S. R. & Zhang, Y. S. Microfluidic integration of regeneratable electrochemical affinity-based biosensors for continual monitoring of organ-on-a-chip devices. *Nat. Protoc.* **16**, 2564–2593 (2021).

131. Zhang, Y. S. et al. Multisensor-integrated organs-on-chips platform for automated and continual in situ monitoring of organoid behaviors. *Proc. Natl Acad. Sci. USA* **114**, E2293–E2302 (2017).

132. Kaisti, M. Detection principles of biological and chemical FET sensors. *Biosens. Bioelectron.* **98**, 437–448 (2017).

133. Shaegh, S. A. M. et al. A microfluidic optical platform for real-time monitoring of pH and oxygen in microfluidic bioreactors and organ-on-chip devices. *Biomicrofluidics* **10**, 044111 (2016).

134. Usuba, R. et al. Photonic lab-on-a-chip for rapid cytokine detection. *ACS Sens.* **1**, 979–986 (2016).

135. Luchansky, M. S. & Bailey, R. C. Rapid, multiparameter profiling of cellular secretion using silicon photonic microring resonator arrays. *J. Am. Chem. Soc.* **133**, 20500–20506 (2011).

136. Podoleanu, A. G. Optical coherence tomography. *J. Microsc.* **247**, 209–219 (2012).

137. Braaf, B. et al. in *High Resolution Imaging in Microscopy and Ophthalmology: New Frontiers in Biomedical Optics* Ch. 7 (Springer, 2019).

138. Arik, Y. B. et al. Microfluidic organ-on-a-chip model of the outer blood–retinal barrier with clinically relevant read-outs for tissue permeability and vascular structure. *Lab Chip* **21**, 272–283 (2021).

139. Pauty, J. et al. A vascular endothelial growth factor-dependent sprouting angiogenesis assay based on an in vitro human blood vessel model for the study of anti-angiogenic drugs. *EBioMedicine* **27**, 225–236 (2018).

140. Dalmay, C. et al. Ultra sensitive biosensor based on impedance spectroscopy at microwave frequencies for cell scale analysis. *Sens. Actuators A Phys.* **162**, 189–197 (2010).

141. Artis, F. et al. Microwaving biological cells: intracellular analysis with microwave dielectric spectroscopy. *IEEE Microw. Mag.* **16**, 87–96 (2015).

142. Grenier, K. et al. Recent advances in microwave-based dielectric spectroscopy at the cellular level for cancer investigations. *IEEE Trans. Microw. Theory Tech.* **61**, 2023–2030 (2013).

143. Kelleci, M., Aydogmus, H., Aslanbas, L., Erbil, S. O. & Selim Hanay, M. Towards microwave imaging of cells. *Lab Chip* **18**, 463–472 (2018).

144. Jang, C., Park, J.-K., Lee, H.-J., Yun, G.-H. & Yook, J.-G. Sensitivity-enhanced fluidic glucose sensor based on a microwave resonator coupled with an interferometric system for noninvasive and continuous detection. *IEEE Trans. Biomed. Circuits Syst.* **15**, 1017–1026 (2021).

145. Zarifi, M. H., Sadabadi, H., Hejazi, S. H., Daneshmand, M. & Sanati-Nezhad, A. Noncontact and nonintrusive microwave-microfluidic flow sensor for energy and biomedical engineering. *Sci. Rep.* **8**, 139 (2018).

146. Peytral-Rieu, O., Dubuc, D. & Grenier, K. Microwave-based sensor for the noninvasive and real-time analysis of 3-D biological microtissues: microfluidic improvement and sensitivity study. *IEEE Trans. Microw. Theory Tech.* **71**, 4996–5003 (2023).

147. Wikswo, J. P. et al. Scaling and systems biology for integrating multiple organs-on-a-chip. *Lab Chip* **13**, 3496–3511 (2013).

148. Herland, A. et al. Quantitative prediction of human pharmacokinetic responses to drugs via fluidically coupled vascularized organ chips. *Nat. Biomed. Eng.* **4**, 421–436 (2020).

149. Pollet, A. M. A. O. & den Toonder, J. M. J. Recapitulating the vasculature using organ-on-chip technology. *Bioengineering* **7**, 17 (2020).

150. Gao, W. et al. One-step formation of protein-based tubular structures for functional devices and tissues. *Adv. Healthc. Mater.* **10**, e2001746 (2021).

151. Helander, H. F. & Fändriks, L. Surface area of the digestive tract—revisited. *Scand. J. Gastroenterol.* **49**, 681–689 (2014).

152. Hasan, M. & Ferguson, A. Measurements of intestinal villi in non-specific and ulcer-associated duodenitis—correlation between area of microdissected villus and villus epithelial cell count. *J. Clin. Pathol.* **34**, 1181–1186 (1981).

153. Marsh, M. N. & Swift, J. A. A study of the small intestinal mucosa using the scanning electron microscope. *Gut* **10**, 940–949 (1969).

154. Trbojević-Stanković, J. B. et al. Morphometric study of healthy jejunal and ileal mucosa in adult and aged subjects. *Histol. Histopathol.* **25**, 153–158 (2010).

155. Lin, F. Y. et al. Cardiac chamber volumes, function, and mass as determined by 64-multidetector row computed tomography. *JACC Cardiovasc. Imaging* **1**, 782–786 (2008).

156. Adler, D. H. et al. Characterizing the human hippocampus in aging and Alzheimer's disease using a computational atlas derived from ex vivo MRI and histology. *Proc. Natl Acad. Sci. USA* **115**, 4252–4257 (2018).

157. Nowakowski, T. J., Pollen, A. A., Sandoval-Espinosa, C. & Kriegstein, A. R. Transformation of the radial glia scaffold demarcates two stages of human cerebral cortex development. *Neuron* **91**, 1219–1227 (2016).

158. Popel, A. S. & Johnson, P. C. Microcirculation and hemorheology. *Annu. Rev. Fluid Mech.* **37**, 43–69 (2005).

159. Callaghan, F. M. & Grieve, S. M. Normal patterns of thoracic aortic wall shear stress measured using four-dimensional flow MRI in a large population. *Am. J. Physiol. Heart Circ. Physiol.* **315**, H1174–H1181 (2018).

160. Dobrin, P. B. Mechanical properties of arteries. *Physiol. Rev.* **58**, 397–460 (1978).

161. Morrison, T. M., Choi, G., Zarins, C. K. & Taylor, C. A. Circumferential and longitudinal cyclic strain of the human thoracic aorta: age-related changes. *J. Vasc. Surg.* **49**, 1029–1036 (2009).

162. Dutton, J. S., Hinman, S. S., Kim, R., Wang, Y. & Allbritton, N. L. Primary cell-derived intestinal models: recapitulating physiology. *Trends Biotechnol.* **37**, 744–760 (2019).

163. Park, J. et al. Three-dimensional brain-on-a-chip with an interstitial level of flow and its application as an in vitro model of Alzheimer's disease. *Lab Chip* **15**, 141–150 (2015).

164. Lindstrøm, E. K., Ringstad, G., Mardal, K. A. & Eide, P. K. Cerebrospinal fluid volumetric net flow rate and direction in idiopathic normal pressure hydrocephalus. *NeuroImage Clin.* **20**, 731–741 (2018).

165. Basson, M. D. Paradigms for mechanical signal transduction in the intestinal epithelium. *Digestion* **68**, 217–225 (2003).

166. McCain, M. L., Yuan, H., Pasqualini, F. S., Campbell, P. H. & Parker, K. K. Matrix elasticity regulates the optimal cardiac myocyte shape for contractility. *Am. J. Physiol. Heart Circ. Physiol.* **306**, 1525–1539 (2014).

167. Carreau, A., Hafny-Rahbi, B. E. L., Matejuk, A., Grillon, C. & Kieda, C. Why is the partial oxygen pressure of human tissues a crucial parameter? Small molecules and hypoxia. *J. Cell. Mol. Med.* **15**, 1239–1253 (2011).

168. Ast, T. & Mootha, V. K. Oxygen and mammalian cell culture: are we repeating the experiment of Dr. Ox? *Nat. Metab.* **1**, 858–860 (2019).

169. Winegrad, S., Henrion, D., Rappaport, L. & Samuel, J. L. Self-protection by cardiac myocytes against hypoxia and hyperoxia. *Circ. Res.* **85**, 690–698 (1999).

170. Erecińska, M. & Silver, I. A. Tissue oxygen tension and brain sensitivity to hypoxia. *Respir. Physiol.* **128**, 263–276 (2001).

171. Winkler, E. A. et al. A single-cell atlas of the normal and malformed human brain vasculature. *Science* **375**, eabi7377 (2022).

172. Wang, Y. et al. Single-cell transcriptome analysis reveals differential nutrient absorption functions in human intestine. *J. Exp. Med.* **217**, e20191130 (2019).

173. Tucker, N. R. et al. Transcriptional and cellular diversity of the human heart. *Circulation* **142**, 466–482 (2020).

174. Litviňuková, M. et al. Cells of the adult human heart. *Nature* **588**, 466–472 (2020).

175. Miterko, L. N., Lackey, E. P., Heck, D. H. & Sillitoe, R. V. Shaping diversity into the brain's form and function. *Front. Neural Circuits* **12**, 83 (2018).

176. Bhaduri, A. et al. An atlas of cortical arealization identifies dynamic molecular signatures. *Nature* **598**, 200–204 (2021).

177. Siletti, K. et al. Transcriptomic diversity of cell types across the adult human brain. *Science* **382**, eadd7046 (2024).

178. Velmeshev, D. et al. Single-cell analysis of prenatal and postnatal human cortical development. *Science* **382**, eadf0834 (2024).

179. Mathiisen, T. M., Lehre, K. P., Danbolt, N. C. & Ottersen, O. P. The perivascular astroglial sheath provides a complete covering of the brain microvessels: an electron microscopic 3D reconstruction. *Glia* **58**, 1094–1103 (2010).

180. Armulik, A., Genové, G. & Betsholtz, C. Pericytes: developmental, physiological, and pathological perspectives, problems, and promises. *Dev. Cell* **21**, 193–215 (2011).

181. Wang, Y. F., Liu, C. & Xu, P. F. Deciphering and reconstitution of positional information in the human brain development. *Cell Regen.* **10**, 29 (2021).

182. Alonso-Nanclares, L., Gonzalez-Soriano, J., Rodriguez, J. R. & DeFelipe, J. Gender differences in human cortical synaptic density. *Proc. Natl Acad. Sci. USA* **105**, 14615–14619 (2008).

183. Gonon, F. Prolonged and extrasynaptic excitatory action of dopamine mediated by D1 receptors in the rat striatum in vivo. *J. Neurosci.* **17**, 5972–5978 (1997).

184. Calandra, T., Gerain, J., Heumann, D., Baumgartner, J. D. & Glauser, M. P. High circulating levels of interleukin-6 in patients with septic shock: evolution during sepsis, prognostic value, and interplay with other cytokines. *Am. J. Med.* **91**, 23–29 (1991).

185. Leng, F. & Edison, P. Neuroinflammation and microglial activation in Alzheimer disease: where do we go from here? *Nat. Rev. Neurol.* **17**, 157–172 (2021).

186. Yuan, W., Lv, Y., Zeng, M. & Fu, B. M. Non-invasive measurement of solute permeability in cerebral microvessels of the rat. *Microvasc. Res.* **77**, 166–173 (2009).

187. Nejdfors, P., Ekelund, M., Jeppsson, B. & Weström, B. R. Mucosal in vitro permeability in the intestinal tract of the pig, the rat, and man: species- and region-related differences. *Scand. J. Gastroenterol.* **35**, 501–507 (2000).

188. Nunes, S. S. et al. Biowire: a platform for maturation of human pluripotent stem cell-derived cardiomyocytes. *Nat. Methods* **10**, 781–787 (2013).

189. Zhao, Y. et al. Towards chamber specific heart-on-a-chip for drug testing applications. *Adv. Drug Deliv. Rev.* **165–166**, 60–76 (2020).

190. Gyorgy, B. & Andreas, D. Neuronal oscillations in cortical networks. *Science* **304**, 1926–1929 (2004).

191. Darwich, A. S., Aslam, U., Ashcroft, D. M. & Rostami-Hodjegan, A. Meta-analysis of the turnover of intestinal epithelia in preclinical animal species and humans. *Drug Metab. Dispos.* **42**, 2016–2022 (2014).

192. Moutairou, K. et al. Epithelial cell migration on small intestinal villi in the neonatal rat. Comparison between [³H] thymidine and cytoplasmic labelling after Pu-citrate ingestion. *Biol. Cell* **65**, 265–269 (1989).

193. Parker, A. et al. Cell proliferation within small intestinal crypts is the principal driving force for cell migration on villi. *FASEB J.* **31**, 636–649 (2017).

194. Zhao, Y. et al. A platform for generation of chamber-specific cardiac tissues and disease modeling. *Cell* **176**, 913–927 (2019).

195. Mathur, A. et al. Human iPSC-based cardiac microphysiological system for drug screening applications. *Sci. Rep.* **5**, 8883 (2015).

196. Narang, R. et al. Sensitive, real-time and non-intrusive detection of concentration and growth of pathogenic bacteria using microfluidic-microwave ring resonator biosensor. *Sci. Rep.* **8**, 15807 (2018).

Acknowledgements

Author contributions

Competing interests

Additional information

[1]Leiden University Medical Center, Leiden, the Netherlands. [2]University Medical Center Groningen, University of Groningen, Groningen, the Netherlands. [3]Delft University of Technology, Delft, the Netherlands. [4]Erasmus University Medical Center, Rotterdam, the Netherlands. [5]Hubrecht Institute, Royal Netherlands Academy of Arts and Sciences (KNAW) and UMC Utrecht, Utrecht, the Netherlands. [6]University of Twente, Enschede, the Netherlands. [7]These authors contributed equally: Dennis M. Nahon, Renée Moerkens. ✉e-mail: c.l.mummery@lumc.nl